Femtosecond transient-grating techniques: Population and coherence dynamics involving ground and excited states

Emily J. Brown, Qingguo Zhang,[a] and Marcos Dantus[b]
Department of Chemistry and Center for Fundamental Materials Research, Michigan State University, East Lansing, Michigan 48824-1322

(Received 11 May 1998; accepted 23 December 1998)

Time-resolved transient grating techniques (TG) arising from four-wave mixing (FWM) processes are explored for the study of molecular dynamics in gas-phase systems ranging from single atoms to large polyatomic molecules. For atomic species such as Ar and Xe, each TG signal shows only a peak at zero time delay when all three incident pulses are overlapped temporally. For diatomic O_2 and N_2 and linear triatomic CS_2 molecules, the TG signals exhibit ground state rotational wave packet recurrences that can be analyzed to obtain accurate rotational constants for these molecules. With heavier systems such as HgI_2, ground state vibrational and rotational wave packet dynamics are observed. Resonant excitation allows us to select between measurements that monitor wave packet dynamics, i.e., populations in the ground or excited states or coherences between the two electronic states. To illustrate these two cases we chose the $X \rightarrow B$ transition in I_2. TG measurements yield dynamic information characteristic of vibrational and rotational wave packets from the ground and excited states. Reverse transient grating (RTG) experiments monitor the time evolution of an electronic coherence between the ground and excited states which includes vibrational and rotational information as well. Early time TG signal for the polyatomic samples CH_2Cl_2, CH_2Br_2, benzene, and toluene exhibit a coherence coupling feature at time zero followed by rotational dephasing. Differences in the amplitude of these two components are related to the contributions from the isotropic and anisotropic components of the molecular polarizability. A theoretical formalism is developed and used successfully to interpret and simulate the experimental transients. The measurements in this study provide gas-phase rotational and vibrational dephasing information that is contrasted, in the case of CS_2, with liquid-phase measurements. This comparison provides a time scale for intramolecular dynamics, intermolecular collisions, and solvation dynamics. © *1999 American Institute of Physics.* [S0021-9606(99)02012-7]

I. INTRODUCTION

The past decade has witnessed rapid growth of real-time molecular dynamics investigation using ultrashort laser pulses.[1–4] Various probing techniques have been exploited in this endeavor. Particularly, third- or higher-order nonlinear techniques have been employed increasingly in recent years for studying molecular dynamics in the gas-phase environment. Techniques similar to coherent transient birefringence in vapor samples, pioneered by Heritage *et al.* in the picosecond regime,[5] were recognized by Fayer and co-workers for their potential for probing gas-phase dynamics.[6–8] Examples of such novel techniques extended to the femtosecond time scale include degenerate four-wave mixing (DFWM)[9,10] and coherent anti-Stokes Raman scattering (CARS).[11,12] In this study, we examine the different types of dynamics that can be observed by time-resolved transient-grating (TG) techniques involving four-wave mixing (FWM) nonlinear optical processes. The name ''transient grating'' is used here to highlight the fact that most of the information obtained in these experiments derives from the time-ordering of various ultrashort pulses and not from high-resolution frequency tuning. We explore the TG signals from a series of atomic, diatomic, and polyatomic systems. A theoretical framework is included that takes into account the different third-order nonlinear processes that contribute to the observed signals. From this analysis formulae are derived to analyze the vibrational and rotational dynamics observed in the experimental transients for both resonant and off-resonant excitation.

Most ultrafast experiments on molecular dynamics in the gas phase have been carried out using the pump–probe technique.[1–4] In these experiments, a pump laser initiates the dynamics of a system typically through a one-photon excitation process. In a few studies multiphoton excitation by the pump laser has been utilized to access higher-lying electronic or vibrational states.[13–17] For the probe process, various techniques have been used; examples include linear techniques such as absorption and laser induced fluorescence (LIF) and nonlinear techniques such as fluorescence upconversion and multiphoton excitation followed by photoionization or photoelectron detection.[1–4] The formalisms for quantitative analysis of these measurements, i.e., the extraction of vibrational and rotational populations, are well known.[18–20] One of the goals of this work is to extend this level of understanding to the quantitative analysis of ultrafast

[a]Current address: George R. Harrison Spectroscopy Laboratory, Massachusetts Institute of Technology, Cambridge, Massachusetts 02139.
[b]Author to whom correspondence should be addressed. Electronic mail address: dantus@cem.msu.edu.

 © 1999 American Institute of Physics

molecular dynamics measured by gas-phase transient grating experiments arising from four-wave mixing nonlinear processes.

Although time-resolved third-order nonlinear optical techniques have long been used in condensed phases,[21–34] only recently have these novel probes been applied to the study of femtosecond dynamics in the gas phase.[9–12] Hayden and Chandler used femtosecond time-resolved CARS to study coherent rotational dephasing of large gas-phase molecules.[11] Zewail and co-workers used DFWM for probing real-time reaction dynamics.[9] They demonstrated three types of arrangements: DFWM, pump pulse followed by DFWM probing, and pump pulse followed by a control pulse with the depletion dynamics probed by DFWM. Schmitt *et al.* have studied iodine vapor using time-resolved CARS and DFWM.[10,12,35,36] By varying the time delay of one of the incident pulses while maintaining the other two incident pulses fixed, they showed that vibrational and rotational dynamics can be observed for both the ground and excited electronic states.

The time resolution of four-wave mixing measurements depends on two different parameters. The first is related to the time duration of the laser pulses interrogating the sample. The second is related to the coherence time of the laser pulses, i.e., the Fourier transform of the spectral width of the laser.[37] The observation of femtosecond vibrational dynamics can be achieved with nanosecond laser pulses provided they have a broad spectral bandwidth.[38] Experiments using nanosecond sources obtain purely the information that is contained in the steady-state absorption spectrum, which is Fourier transformed and convolved by the coherence length of the light source. The easy availability of broad-band light sources with extremely short coherence lengths make those kinds of measurements, which are similar to Fourier transform infrared spectroscopy, very attractive.[38] However, it is worth noting the advantages of experiments obtained with femtosecond pulses. For these experiments, the laser interrogation of the sample is complete within a time-scale that is short compared to various dephasing mechanisms. Therefore, by using femtosecond pulses in FWM measurements, (a) the onset of electronic vibrational and rotational dephasing can be directly observed,[39] (b) there is a possibility to control the temporal ordering of the three electric fields and their relative phases,[40] (c) four-wave mixing and six-wave mixing are easily accessible because of the nonlinear dependence of these techniques on laser intensity,[41] (d) frequency chirps can be used to control the wave packet that is launched by each laser interaction with the sample,[42] and (e) for chemical reactions one is able to interrogate the transition states, i.e., observe as the reactants become products. The additional sensitivity gained with ultrashort pulses makes off-resonant measurements easily accessible.

Here we report a systematic study of femtosecond time-resolved transient-grating experiments on atomic, diatomic, triatomic, and larger molecular systems. Our goal is to demonstrate the various types of molecular dynamics accessible and to provide a semiempirical formalism to extract quantitative information from TG and related four-wave mixing nonlinear optical signals. After a description of theory and experimental arrangements in Secs. II and III, the focus will turn to presenting and interpreting the various types of TG transients observed experimentally.

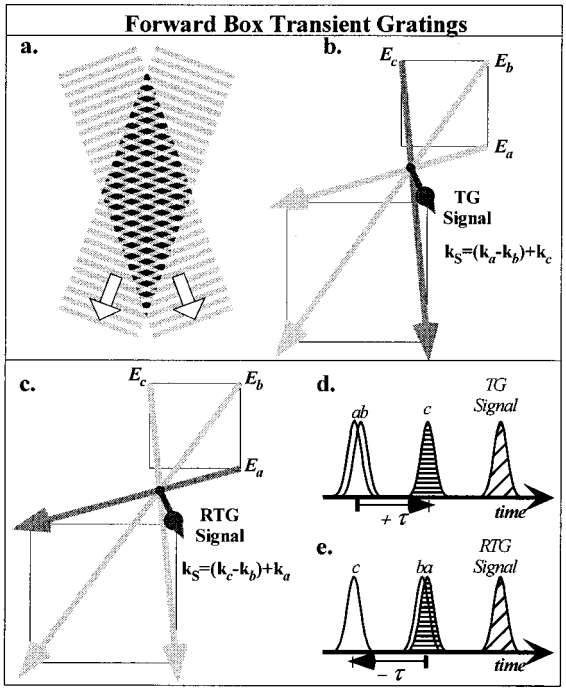

FIG. 1. Gratings formed in the forward box configuration. (a) Formation of a transient grating by two electric fields. Note that the direction of the grating bisects the angle between the fields. Areas of higher absolute electric field are darker. (b) Grating formed between E_a and E_b. Note that E_c Bragg scatters into the upper right corner resulting in the signal-beam. This occurs for $\tau \geqslant 0$. (c) Grating formed between E_b and E_c. Note that E_a Bragg scatters into the upper right corner resulting in the signal-beam. This occurs for $\tau \leqslant 0$. (d) Schematic of the pulse sequence in TG measurements. For this case, positive τ, the grating is formed by fields E_a and E_b. This signal arises from the scattering of field E_c. (e) Schematic of the pulse sequence in RTG measurements. For this case, negative τ, the grating is formed by fields E_c and E_b. This signal arises from the scattering of field E_a.

II. THEORY

Theoretical treatments of time-dependent four-wave mixing signals are abundant in the literature.[37,43] Here, a review of the results relevant to this study will be presented.

A. General considerations

One of the most physically intuitive explanations of time-resolved four-wave mixing techniques is based on the formation of transient gratings by the incident lasers.[6,44,45] Consider three incident light pulses with electric fields $E_a(t)$, $E_b(t)$, and $E_c(t)$ interacting with a medium. From here on we will assume that the three fields are identical in terms of pulse envelope and frequency components, i.e., they are degenerate; however, this is not to be considered as a necessary condition. At the crossing of two beams, the spatial modulation of their electric fields varies due to constructive and destructive interference [see Fig. 1(a)]. The molecules in the interaction region experience varying electric field intensities according to their position and this leads to the formation of a transient grating of polarized molecules in space. The formation of the grating does not require that the

two crossing beams coincide in time as long as the coherence is maintained in the sample.[46] This property has been exploited in photon echo experiments where the time delay between the lasers is used to probe the coherence dephasing time.[37,47–50] The transient grating formation can be probed easily by the detection of Bragg scattering of a third laser beam.[6,44,45]

Experimentally, there are various configurations that can be used to observe the FWM signal. For our studies, we have chosen the forward box arrangement as shown in Fig. 1 because it provides the best temporal resolution and phase matching between the incident fields.[51,52] For all cases, the FWM signal that is detected at the upper right corner of the forward box, as shown in Fig. 1, is defined by the wave vector $\mathbf{k}_s=\mathbf{k}_a-\mathbf{k}_b+\mathbf{k}_c$. Note that other FWM signals are possible and they are observable in other directions. In this manuscript we restricted our measurements such that E_a and E_b are coincident in time and E_c is scanned. When fields E_a and E_b precede E_c, it is called positive time; negative time refers to field E_c preceding E_a and E_b. In Sec. II B we describe the transient gratings formed in these two cases.

Based on the relative timing of the three fields, one can envision three types of gratings being formed.[44,45,53] The first one, shown in Fig. 1(b), involves E_a and E_b forming a grating in the horizontal plane from which E_c scatters for positive delay times, τ. The second arrangement, shown in Fig. 1(c), involves E_c and E_b forming a grating in the vertical plane with subsequent scattering of E_a. More information about this latter configuration, known as reverse transient grating (RTG),[54] will be given later. The third grating is formed by E_a and E_c in a diagonal plane, but scattering of E_b takes place in the direction $\mathbf{k}_s=\mathbf{k}_a-\mathbf{k}_c+\mathbf{k}_b$ which does not coincide spatially with $\mathbf{k}_s=\mathbf{k}_a-\mathbf{k}_b+\mathbf{k}_c$. The medium that constitutes the gratings discussed so far is composed of the sample molecules that in the gas phase move freely. Therefore, molecular dynamics cause the decay and reformation of the transient grating. Here we theoretically and experimentally explore the ground and excited states vibrational and rotational populations and the coherence dynamics from gas-phase samples probed by these time-resolved four-wave mixing techniques.

The FWM signal intensity, $I_{\mathrm{FWM}}(\tau)$, resulting from the interaction between the three incident laser pulses and the sample medium, can be evaluated using[37,43,55]

$$I_{\mathrm{FWM}}(\tau)=\int_{-\infty}^{\infty}|P^{(3)}(\mathbf{k}_s,t)|^2dt, \tag{1}$$

where $P^{(3)}(\mathbf{k}_s,t)$ represents the time-dependent third-order polarization for a given phase matching condition. This equation is applicable for homodyne detection. For TG measurements with $\mathbf{k}_s=\mathbf{k}_a-\mathbf{k}_b+\mathbf{k}_c$, $P^{(3)}(\mathbf{k}_s,t)$ can be expressed as[37]

$$P^{(3)}(\mathbf{k}_s,t)=-E_2(t)\int_0^{\infty}|E_1(\tau-t')|^2\chi^{(3)}(t')dt', \tag{2}$$

where $\chi^{(3)}(t)$ is the third order susceptibility associated with the molecular system, E_1 is the electric field of the pulses forming the transient grating, and E_2 is the electric field that scatters from the transient grating. In order to determine what type of information should be included in the molecular susceptibility term, it is important to first analyze the different interactions that are possible between the laser fields and the sample.

Calculation of the FWM polarization $P^{(3)}(\mathbf{k}_s,t)$ and associated susceptibility requires knowledge of the third-order density operator $\rho^{(3)}(t)$.[37,43] The explicit form of $\rho^{(3)}(t)$ follows from a perturbative solution of the quantum mechanical Liouville equation that describes the temporal evolution of the system under the influence of the incident electromagnetic fields and the intrinsic relaxation processes.[37,43] This analysis is illustrated schematically by the double-sided Feynman diagrams in Fig. 2. The diagrams shown are based on those by Shen, Mukamel, and Vaccaro who have explained in great detail the use of these diagrams for the understanding of nonlinear spectroscopy.[37,43,56] Simplier diagrams that alternate up and down transitions between two states often fail to describe differences between populations and coherences, *vide infra*.

B. Resonant excitation

First we consider the case in which the three laser fields are resonant with a two-level system. The diagrams shown in Fig. 2 are representations of the time evolution of the density matrix operator ρ and its transformations by the interaction with the electric fields. The operator is denoted by the two parallel arrows which correspond to the bra $\langle g|$ (on the right) and the ket $|g\rangle$ (on the left) of the matrix. Time increases from the bottom to the top. Wavy arrows represent the interaction of each of the fields E_j with the sample. Those pointing towards the right correspond to $E_j\exp(-i\omega_j t+i\mathbf{k}_j\cdot\mathbf{r})$, while those pointing left correspond to $E_j^*\exp(i\omega_j t-i\mathbf{k}_j\cdot\mathbf{r})$. The sign of the first term in these expressions, $\pm i\omega_j t$, is used to indicate absorption or emission of a photon. Because the bra and ket are in dual correspondence to each other—a complex prefactor on a ket appears as the complex conjugate prefactor on the corresponding bra.[57] Therefore, arrows pointing towards the center of the diagram indicate photon absorption while those pointing away indicate photon emission. Detection of signal from a particular phase matching configuration, for example, $\mathbf{k}_s=\mathbf{k}_a-\mathbf{k}_b+\mathbf{k}_c$ as shown in Fig. 1, determines the sign of the individual wave vectors. Therefore, for all diagrams fields E_a and E_c must be represented with right pointing arrows, $+\mathbf{k}_j$, and field E_b with a left pointing arrow, $-\mathbf{k}_j$.

The first field interaction may involve any one of the three fields acting on the bra or ket side. This results in six possible alternatives. The second interaction may involve either of the two remaining fields acting on the bra or ket side, giving a total of 6×4 alternatives. Finally the remaining field can act on the bra or ket side giving a total of 48 possible diagrams, representing the transformation of the initially incoherent ground state medium $\rho^{(0)}$ into $\rho^{(3)}(t)$ for this phase matching condition.[37,43,56]

For resonant or near-resonant excitation, not all 48 diagrams contribute to the observed signal. In fact the rotating wave approximation (RWA) can be used to rule out most of these combinations.[58] First we define the transition frequency

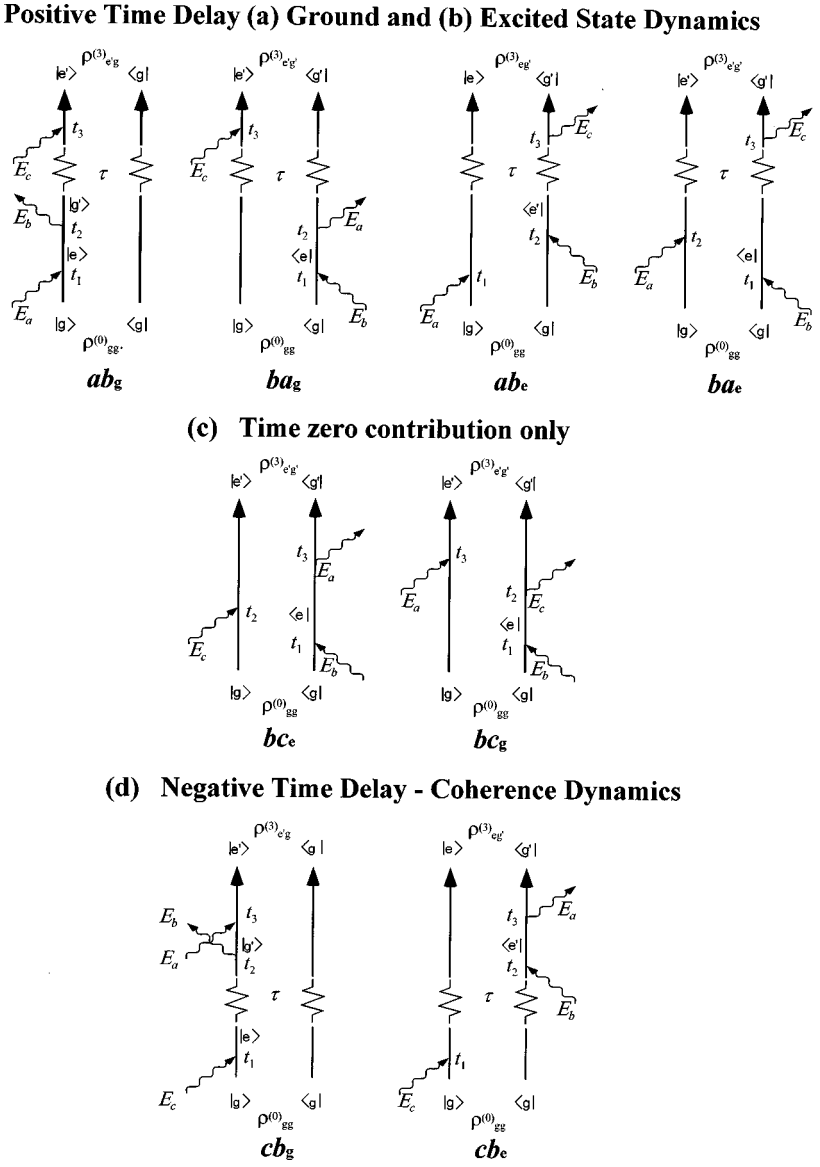

FIG. 2. Double-sided Feynman diagrams corresponding to four-wave mixing processes observed for phase matching condition $\mathbf{k}_s=\mathbf{k}_a-\mathbf{k}_b+\mathbf{k}_c$. In all cases the signal, emission from the ket side, has been omitted for clarity. Based on the experimental constraints of our measurements, beams E_a and E_b are overlapped in time and beam E_c can be delayed or advanced with respect to these beams. The label for each diagram, for example ab_g, indicates the two beams that form the transient grating and the state in which the population is formed. (a) For positive time delays, E_a and E_b form the grating and cause a transformation of $\rho_{gg}^{(0)}$ into $\rho_{g'g}^{(2)}$ or $\rho_{gg'}^{(2)}$. When E_c scatters from this grating, at positive time, ground state dynamics are obtained. (b) Here E_a and E_b form the grating and cause a transformation of $\rho_{gg}^{(0)}$ into $\rho_{ee'}^{(2)}$ or $\rho_{e'e}^{(2)}$. When E_c scatters from this grating, at positive time, excited state dynamics are obtained. (c) These diagrams contain beam E_c between fields E_a and E_b which are overlapped in time. Therefore signal is observed only for times within the laser pulse duration. (d) For these diagrams E_c arrives first and, if resonant, forms a coherence between the ground and excited states of the form $\rho_{eg}^{(1)}$. The coherence is allowed to evolve for a time τ. The coherence dynamics are probed by the arrival of field E_b, which forms the grating, and field E_a that scatters from the grating.

$\Omega_{eg}=-\Omega_{ge}$ corresponding to the energy difference between the ground and the excited states; therefore, near-resonant excitation has $\omega_j\approx\Omega_{eg}$, where ω_j is the photon frequency. When field E_a acts on the ket at time t_1, the corresponding contribution to the susceptibility is proportional to $\langle e|\mu\cdot E_a|g\rangle/(\Omega_{eg}-\omega_a)$. When the denominator is small, in this case near zero, the contribution is large. However, if E_a acts on the bra at time t_1, the corresponding denominator is $(\Omega_{ge}-\omega_a)=(-\Omega_{eg}-\omega_a)$, about twice the optical frequency. Contributions from these antirotating wave processes are very small and can be neglected for weak near-resonant fields. One can identify eight of the 48 diagrams in which all three field interactions satisfy the RWA and therefore these eight diagrams have a significant contribution to the susceptibility. This selection process has been documented in the literature.[37,56,59]

The diagrams shown in Fig. 2 assume near-resonant excitation between two states, labeled here g and e. Some of the differences expected for non-resonant excitation are pointed out later in the discussion. Time ordering of each field is given by the relative vertical position of the wavy arrows and by the time labels t_1, t_2, and t_3. In all eight cases the last step, corresponding to emission of the signal field from the ket side, has been omitted to simplify these diagrams. The transformation of $\rho^{(0)}=|g\rangle\langle g|$, designated as $\rho_{gg}^{(0)}$, following each laser-sample interaction is labeled on the bra or the ket side. For resonant excitation it is important to illustrate how the susceptibility tensor for an isolated two level system depends on the laser's frequency. The first diagram (ab_g) in Fig. 2 depicts the transformation $\rho_{gg}^{0}\rightarrow\rho_{eg}^{(1)}\rightarrow\rho_{g'g}^{(2)}\rightarrow\rho_{e'g}^{(3)}$. The nonlinear susceptibility associated with this particular interaction between the three laser fields can be expressed as[56]

$$\chi_{ab_g}^{(3)}\propto N\sum_{gg',ee'}\rho_{gg}^{(0)}\times\frac{\langle g|\boldsymbol{\mu}\cdot\mathbf{E}_s^*|e'\rangle\langle e'|\boldsymbol{\mu}\cdot\mathbf{E}_c|g'\rangle\langle g'|\boldsymbol{\mu}\cdot\mathbf{E}_b^*|e\rangle\langle e|\boldsymbol{\mu}\cdot\mathbf{E}_a|g\rangle}{(\Omega_{eg}-\omega_a)(\Omega_{g'g}-\omega_a+\omega_b)(\Omega_{e'g}-\omega_a+\omega_b-\omega_c)}. \quad (3)$$

Notice that once this expression for the susceptibility is introduced in Eqs. (1) and (2), the overall FWM signal depends on the square of the number density of the sample N and the eighth power of the transition dipole μ. Frequency-resolved DFWM techniques have been proven to yield very high-resolution spectra, especially for Doppler-free configurations, taking advantage of the very large resonant enhancement.[53,60]

The eight diagrams have been divided into four groups. The first group, shown in Fig. 2(a), represents the four-wave mixing process allowing the observation of ground state population dynamics. The diagonal terms of the density matrix, ρ_{gg} and ρ_{ee}, are associated with populations while the off-diagonal terms represent coherences. The two diagrams, labeled ab_g and ba_g, indicate transient grating formation in the ground state $\rho^{(2)}_{g'g}$ or $\rho^{(2)}_{gg'}$ by fields E_a and E_b followed by scattering of E_c after a time delay τ indicated by a break in the time arrows.

The second group of diagrams in Fig. 2(b) depicts the observation of excited state dynamics at positive time delays. This observation requires that the excited state is long-lived compared to the pulse width of the laser and that the laser pulses are near-resonant with the electronic transitions. For the two diagrams, labeled ab_e and ba_e, transient grating formation in the excited state $\rho^{(2)}_{ee'}$ or $\rho^{(2)}_{e'e}$ by E_a and E_b is followed by scattering of E_c after a time delay τ. Figure 1(d) shows the pulse sequence that gives the TG signals arising from the diagrams shown in Figs. 2(a) and 2(b).

The third group of diagrams in Fig. 2(c) contains the two sequences in which E_c, the field that can be physically delayed in time in our experimental setup, interacts with the system after field E_b but before field E_a. The signal arising from these interactions, labeled bc_e and bc_g, is therefore limited to near-zero time delays because fields E_a and E_b coincide in time for all experiments in this study. The dynamics observed for different pulse sequences have been explored in our group and will be published elsewhere.[40]

The fourth group of diagrams in Fig. 2(d) corresponds to observations of signals for negative time delays, i.e., when field E_c precedes the other two fields [see also Fig. 1(e) corresponding to the RTG pulse sequence]. The first step in these two diagrams is the formation of a coherence (off-diagonal term in the density matrix) $\rho^{(1)}_{eg}$ between the ground and excited states. After a time delay τ a transient grating population is formed by field E_b in the ground $\rho^{(2)}_{g'g}$ or excited $\rho^{(2)}_{ee'}$ states. Notice that diagrams cb_g and cb_e are identical to ab_g and ab_e expect for the labeling of fields E_a and E_c and thus the relative time ordering of τ. For TG measurements, diagrams ab_g, ba_g, ab_e, and ba_e, the signal depends on ground or excited state population dynamics. For RTG measurements, diagrams cb_g and cb_e, the signal is a measure of the electronic coherence between ground and excited states. The coherence signal decays according to the electronic dephasing time between the states involved, i.e., a T_2 type measurement. In most cases T_2 is very different than T_1, the lifetime of the excited state.[39]

The observation of coherence dynamics for negative time delays is not common to all FWM experiments because it depends on the phase matching configuration, on the polarization of the three incident fields, and on the existence of a resonant or near-resonant state. For experimental arrangements where all three incident beams are in one plane, the direction of the signal wave vector for positive and negative time delays, determined by the phase matching geometry, may be different.[61] The detection geometry can be used to discriminate a particular phase matching geometry. In the forward box arrangements, negative time delay signal is possible [see Fig. 1(c)] for the pulse sequence discussed here and for other sequences.[9,10] When the three incident fields have the same polarization, as in the near-resonant experiment discussed here, the negative time delay signal can be observed. For cases involving nonresonant excitation, excitation of repulsive states, or condensed-phase measurements, a very short coherence lifetime ($\sim 10^{-14}$ s) is expected. Therefore, little or no dynamics are observed for time delays exceeding the laser pulse duration for these systems. Additional discussion on the negative time delay signals can be found in Refs. 54, 62, and 63.

A different diagram classification than the one discussed so far is possible. Notice that for diagrams ba_g, ba_e, bc_e, and bc_g, the first step involves formation of a coherence $\rho^{(1)}_{ge}$. The time evolution of the coherence involves dephasing processes. The dephasing dynamics can be reversed by interaction with the third electric field forming $\rho^{(3)}_{e'g'}$. This reversal, analogous to the $\pi/2$ pulses in nuclear magnetic resonance (NMR), leads to the formation of an echo. Photon echo measurements are extremely useful in the measurement of coherence life times and have been used primarily in the study of relaxation dynamics in condensed phases. For reviews on these studies, see Refs. 64 and 65. These types of measurements require a controlled arrival of field E_b with respect to fields E_a and E_c.

Having sorted out the different molecular responses in FWM experiments, we turn our attention to the types of molecular dynamics that are observed in ground and excited states and how they are manifested in the induced molecular polarization. For TG experiments both ground state and excited state wave packets are formed. The rotational dynamics are given by the time-dependent evolution of the population excited at $t=0$. The molecular orientations are averaged starting with the usual classical expression based on the second Legendre polynomial $P_2[\cos\theta(t)]$, where $\theta(t)$ is the angle between the molecular axis at time t and that at time zero.[66] This evolution has been extensively studied in the time domain for pump–probe time-resolved gas-phase studies by Zewail's research group.[19,67,68] The following semiclassical expression can be used for the quantitative study of the orientational dependent susceptibility and is given by

$$\chi^R(t)=\frac{\Sigma_J P(J)\,\frac{1}{2}(3\cos^2\omega_J t-1)}{\Sigma_J P(J)}$$

$$=\frac{\Sigma_J P(J)\,\frac{1}{4}(1+3\cos 2\omega_J t)}{\Sigma_J P(J)}, \tag{4}$$

where $P(J)$ represents the distribution of rotational levels for the molecules being probed and the rotational frequency ω_j

is given by $2\pi[2Bc(J+1)]$ for $\Delta J=\pm 1$ and $2\pi[4Bc(J+\frac{3}{2})]$ for $\Delta J=\pm 2$ transitions where B is the rotational constant of the molecule in wavenumbers.

The vibrational dynamics can be modeled by a sum of cosine functions each representing the energy difference between adjacent vibrational levels of the ground or excited states. The dependence of the susceptibility on vibrational motion is

$$\chi^{v}(t)=\sum_{i=1}^{3n-5 \text{ or } 3n-6} B_i \cos(\omega_i t+\phi_i), \tag{5}$$

where B_i and ϕ_i are time independent amplitude and phase constants for the ith vibrational mode and ω_i is the fundamental frequency of the ith normal mode. Anharmonicity of each vibrational mode can be included by explicitly adding the frequency of all overtones that are populated in the excitation process. Note that the observation of real-time vibrations requires that the frequency bandwidth of the laser pulses overlap two or more vibrational levels.

In the limit of very short laser pulses, the resonant FWM signal is equal to the square of the sum of the different components of the susceptibility (*vide infra*). Therefore, the third-order resonant TG signal is of the form

$$I_{\text{Resonant}}(\tau)=\left|Ae^{-\tau^2/\Delta^2}+\sum_{i=1}^{3n-5 \text{ or } 3n-6} B_i \cos(\omega_i\tau+\phi_i) + C\beta^2\frac{\Sigma_J P(J)\,\frac{1}{4}(1+3\cos 2\omega_J\tau)}{\Sigma_J P(J)}\right|^2, \tag{6}$$

where A is the amplitude of the time-zero feature that is caused by a contribution from all eight diagrams in Fig. 2, Δ corresponds to the full-width at half-maximum (FWHM) of the coherence time of the laser pulses, i.e., the pulse width divided by $2\sqrt{\ln 2}$ (for Gaussian pulses), and C is a proportionality constant. The second and third terms correspond to vibrational and rotational contributions to the signal. Note that both ground and excited states have to be taken into account for the resonant TG measurements.

For RTG measurements, the dynamics probed involve a coherence between the ground and excited states as discussed above. However, based on the Condon approximation,[37] applicable for resonance excitation only, one can demonstrate that the signal from RTG measurements tracks primarily the excited state. This point is illustrated in a separate communication from our group.[40] For reverse transient gratings, the signals can be modeled by Eq. (6) given for TG measurements. The contribution for the excited state is expected to be about an order of magnitude greater than that of the ground state. An additional term needs to be added to account for the electronic dephasing time T_2 which is long in the gas phase (10^{-12}–10^{-9} s) and very short in condensed phases (10^{-15}–10^{-13} s).

C. Off-resonant excitation

Far from resonance both RWA ($\Omega_{eg}-\omega_j$) and anti-RWA ($\Omega_{eg}+\omega_j$) terms become comparable making the selection of the active Feynman diagrams more difficult. For the particular arrangement discussed here with fields E_a and E_b overlapped in time, diagrams ab_g and ba_g in Fig. 2 illustrate the nonlinear processes responsible for the off-resonant transients. The general principle hinges on impulsive excitation of rotational and vibrational states in the ground state. The polarizability susceptibility of isolated molecules for off-resonant excitation can be expressed as a combination of correlation functions of the effective polarizability of the molecule $\tilde{\alpha}$,[69]

$$\chi^{(3)}(t)=\chi_{\alpha\alpha}(t)=\left\langle\frac{i}{\hbar}[\tilde{\alpha}(t),\tilde{\alpha}(0)]\right\rangle, \tag{7}$$

where $\chi_{\alpha\alpha}$ is the linear response function associated with the molecular polarizability. The polarizability tensor can be expressed by expanding each element in a Taylor series with respect to the normal coordinates of vibration q_i as

$$\tilde{\alpha}=\tilde{\alpha}_0+\sum_{i=1}^{3n-5 \text{ or } 3n-6}\left[\frac{\partial\tilde{\alpha}}{\partial q_i}\right]_0 q_i + \frac{1}{2}\sum_{i,k}^{3n-5 \text{ or } 3n-6}\left[\frac{\partial^2\tilde{\alpha}}{\partial q_i\partial q_k}\right]_0 q_i q_k+\cdots. \tag{8}$$

The first term corresponds to the equilibrium polarizability and can be separated into its isotropic and anisotropic contributions by using the definitions $\alpha\equiv\frac{1}{3}(\alpha_\parallel+2\alpha_\perp)$ and $\beta\equiv(\alpha_\parallel-\alpha_\perp)$. Here $\alpha_\parallel$ and $\alpha_\perp$ are the parallel and perpendicular components of the polarizability with respect to the principal symmetry axis of the molecule. This separation leads to two contributions. The equilibrium isotropic term, having no orientation or vibrational dependence, does not contribute to the observed dynamics except for a time-zero instantaneous response (*vide infra*). The second contribution, corresponding to the equilibrium anisotropic polarizability, depends on the molecular orientation and is therefore responsible for the rotational component which has been expressed as

$$\chi^{R}(t)=-\frac{4N\beta^2}{45k_BT}\frac{\partial}{\partial t}\langle P_2[\cos\theta(t)]\rangle, \tag{9}$$

where N denotes sample density, T is the sample temperature, and k_B is the Boltzmann constant.[69–71] For spherically symmetric molecules having $\beta=\alpha_\parallel-\alpha_\perp=0$, the pure orientational contribution vanishes. Note that the derivative arises from the fact that contributions to the time-dependent polarizability are purely imaginary for off-resonant excitation (purely real in the frequency domain). The expression given here is relevant for the case discussed in this paper where all beams are linearly polarized in the same direction. Different polarization arrangements are discussed elsewhere.[53,69,70] By expressing the ensemble average and the second-order Legendre polynomial as done by Zewail and coworkers,[19,67,68] the last factor in Eq. (9) can be evaluated using

$$\frac{d}{dt}\langle P_2[\cos\theta(t)]\rangle = \frac{d}{dt}\frac{\Sigma_J P(J)\,\frac{1}{2}[3\cos^2\omega_J t-1]}{\Sigma_J P(J)} = -\frac{3}{2}\frac{\Sigma_J P(J)\omega_J \sin 2\omega_J t}{\Sigma_J P(J)}. \quad (10)$$

The effects on the rotational recurrences caused by nuclear spin and centrifugal distortion are discussed in Sec. IV B.

The second term in Eq. (8), corresponding to the derivative of the polarizability in terms of the vibrational coordinates, can be expanded in terms of isotropic and anisotropic contributions. This separation yields[69]

$$\chi_{\rm iso}(t) = \sum_{i=1}^{3n-5 \text{ or } 3n-6}\left[\frac{\partial\alpha}{\partial q_i}\right]_0^2\left\langle\frac{i}{\hbar}[q_i(t),q_i(0)]\right\rangle \quad (11a)$$

and

$$\chi_{\rm aniso}(t) = \langle P_2[\cos\theta(t)]\rangle \times \sum_{i=1}^{3n-5 \text{ or } 3n-6}\left[\frac{\partial\beta}{\partial q_i}\right]_0^2\left\langle\frac{i}{\hbar}[q_i(t),q_i(0)]\right\rangle, \quad (11b)$$

where the first-order expansion terms are given by $[\partial\alpha/\partial q_i]_0$ and $[\partial\beta/\partial q_i]_0$ at the equilibrium internuclear separation. Both of these expressions give the rovibrational dependence of the polarizability. The different isotropic and anisotropic contributions for each normal mode can be sorted by experiments that are sensitive to the polarization of the signal beam for different incoming polarizations.[24,37,53,56,72–78] The focus of our study is on the molecular dynamics; no effort has been made to sort the isotropic and anisotropic components as shown in Eqs. (11a) and (11b).

Because the correlation function for a coherent superposition of vibrational modes is sinusoidal in time, the vibrational contribution $\chi^v(t)$ of Eqs. (11a) and (11b) can be modeled as a summation of sine functions,

$$\chi^v(t) = \sum_{i=1}^{3n-5 \text{ or } 3n-6} B_i \sin(\omega_i t+\phi_i). \quad (12)$$

Notice that in Eq. (12) we have omitted the orientational term due to the anisotropic susceptibility in Eq. (11b). We have also omitted the anharmonic contributions that result from the higher-order terms in Eq. (8). For the different samples studied here, we found this level of approximation to be satisfactory. Additional terms can be introduced when the harmonic approximation is not sufficient to model the experimental data. The amplitude and phase of each vibrational motion in the ground or excited state are left as fitting parameters to be determined during the analysis of the experimental data. Thus by combining the vibrational and rotational contributions, the overall expression for $\chi_{\alpha\alpha}(t)$ becomes

$$\chi_{\alpha\alpha}(t) = \sum_{i=1}^{3n-5 \text{ or } 3n-6} B_i \sin(\omega_i t+\phi_i) + \beta^2\frac{\Sigma_J P(J)\omega_J \sin 2\omega_J t}{\Sigma_J P(J)}. \quad (13)$$

Equation (13) reflects a separation of vibrational and rotational contributions to the anisotropy (at least to first order approximation), a fact that has been long recognized in Raman spectroscopy.[79,80] A similar separation can be achieved for frequency-resolved absorption and fluorescence spectroscopy. For time-resolved FWM experiments with homodyne detection, Eq. (13) leads to cross terms between the rotational and vibrational contributions as will be shown later. Heterodyne detection would give a signal proportional to $P^{(3)}(\mathbf{k}_s,t)$ rather than its square, which would be free from cross-terms of the kind referred to above.[37,71] It is interesting to note that for time-resolved pump–probe experiments the rotational and vibrational contributions are multiplied.[19,67,68] The purely rotational component of the signal is typically isolated by the use of the anisotropy measurement defined by

$$r(t) \equiv \frac{I_\parallel - I_\perp}{I_\parallel + 2I_\perp}, \quad (14)$$

where $I_\parallel$ and $I_\perp$ correspond to the time-resolved transients obtained for parallel and perpendicular pump–probe polarizations.[81] Equation (14) indicates that the orientation dependence multiplies the isotropic molecular dynamics given by $I_\parallel + 2I_\perp$.[67,68,81] For the time-resolved FWM presented here, we demonstrate that this multiplication is no longer applicable for the separation of isotropic and anisotropic contributions to the signal.

For polyatomics, if the polarizability varies as the atoms are displaced collectively along a given normal coordinate, the normal mode is observable by its contribution to $\chi^v(t)$. For linear triatomics of the type ABA, the symmetric stretch satisfies this condition while the antisymmetric stretch and the bend do not. The latter modes are infrared active but are not Raman active. In general, Raman active modes can be observed by four-wave mixing techniques. This point is illustrated in Sec. IV C for HgI_2.

The vibrational selection rules for Raman transitions are determined by integrals of the form

$$\int \psi_{v'}^*\,\alpha_{g,g'}\,\psi_{v''}\,d\tau, \quad (15)$$

where $g,g'=x,y,$ or z, $\alpha_{g,g'}$ is one of the components of the polarizability, and $\psi_{v''}$ and $\psi_{v'}$ refer to the vibrational wave functions in the initial and final states, respectively.[82,83] These integrals vanish unless the vibrational normal mode involved belongs to the same representation as one or more of the six components of the polarizability tensor of the molecule, e.g., α_{xx}, α_{xy}.[84] The rotational Raman selection rule is that the molecule must be anisotropically polarizable (i.e., $\beta=\alpha_\parallel-\alpha_\perp\neq 0$). In addition, for linear molecules ΔJ equals 0, ± 2 and for nonlinear molecules ΔJ can equal 0, ± 1, ± 2.[82]

The observation of rotational and vibrational dynamics for off-resonant measurements depends on the impulsive excitation of vibrational and rotational levels in the ground state, which are overlapped by the frequency bandwidth of the laser pulse. When the vibrational period is shorter than the coherence time of the laser pulse or when all molecules are not vibrating in-phase, the nonlinear response averages to zero and does not contribute to the overall signal. The short

pulses employed in this study are nearly transform limited and have a pulse width of approximately 50 fs. The availability of 5 fs laser pulses[85,86] will extend these types of studies by opening the possibility for observing the real-time dynamics of all but C–H, N–H, and O–H chemical bonds.

Equation (13) gives a satisfactory expression for the susceptibility that can be convolved by the electric fields and squared according to Eqs. (1) and (2) in order to simulate the data. However, in the impulsive limit, when the laser pulse width can be neglected in comparison to the rotational and vibrational periods, the electric field envelopes can be treated essentially as Dirac-delta functions and the FWM signal intensity simply reduces to[37]

$$I_{\mathrm{FWM}}(\tau)=|\chi_{\alpha\alpha}(\tau)|^2. \tag{16}$$

In FWM experiments, when all three fields are present near time zero, a condition of temporal degeneracy arises. During this time multiple nonlinear processes occur. The observed signal enhancement near time zero, arising from the coherent interaction of the three light fields with the medium, has been called the coherence coupling artifact or the coherence spike.[23,37,87–89] The coherent spike is typically symmetric about time zero and in many cases can be removed by the antisymmetrization technique described by Eisenthal, Fleming, and co-workers.[89,90] In the absence of chirp, the coherent spike can be described as the square of the electric field autocorrelation of the incident laser pulses. This is because the major contribution comes from the equilibrium isotropic polarizability (α_0) which has an instantaneous response limited to when the three fields are overlapped in time. For most femtosecond measurements this feature can be approximated by a Gaussian or hyperbolic-secant-squared function. Thus, by considering the coherent spike as a Gaussian function with amplitude A primarily depending on α_0 and using Eqs. (13) and (16), the FWM signal intensity can be modeled as

$$I_{\mathrm{FWM}}(\tau)=\left|Ae^{-\tau^2/\Delta^2}+\sum_{i=1}^{3n-5\ \text{or}\ 3n-6}B_i\sin(\omega_i\tau+\phi_i)+C\beta^2\frac{\Sigma_J P(J)\omega_J\sin 2\omega_J\tau}{\Sigma_J P(J)}\right|^2. \tag{17}$$

For most cases convolution by the temporal response of the laser system can be carried out easily when necessary. This formula is convenient for the analysis of off-resonance TG data. Note that we have not included the inverse-squared dependence of the off-resonance signal on temperature. We hope to derive a more rigorous formula taking into account the full susceptibility tensor in the near future.

This formulation allows the quantitative interpretation of the vibrational and rotational characteristics of the TG off-resonant signals obtained. Atomic species exhibit signals exclusively at time zero because of their instantaneous polarizability. Diatomics and polyatomics exhibit, for positive time delays, ground state rotational (as long as $\beta\neq 0$) and vibrational dynamics. The vibrational modes must be Raman active and have a vibrational period that is longer than the coherence time of the laser system to be observed. In Sec. IV, experimental data is presented to illustrate the different cases discussed. Of particular interest is the experimental observation of the cross terms that arise upon squaring the sum of rotational and vibrational contributions to the signal according to Eqs. (6) and (17). As we will demonstrate later, the off-resonance FWM transients show rotational recurrence features that are quite different from those observed by LIF.[19,67,68,91,92] Most of the differences can be explained in terms of the modulus square and the time derivative in Eqs. (1) and (9).

III. EXPERIMENT

The laser system used for these experiments is a home-built colliding pulse mode-locked dye laser (CPM) pumped by an Ar^+ laser. The output from the CPM is centered at 622 nm and is amplified using a four-stage dye amplifier pumped by a 30 Hz Nd-YAG laser. A double-pass prism pair recompresses the pulses after amplification to produce 50 fs pulses with an average pulse energy of 0.35 mJ. The pulses are confirmed to be transform-limited using a frequency-resolved optical gating (FROG) instrument.

The laser was attenuated by a factor of two and split into three beams of comparable intensity $\sim$50 μJ. The three beams were combined at the sample in the forward box geometry[51,52] by a 0.5 m focal length lens [see Fig. 3(a)]. At the lens focus, the three beams occupied the three corners of a square with 1 in. sides. Each pair of beams were crossed at an angle of 2.6° resulting in a fringe spacing of 14 μm. The beam diameter at the interaction region was 40–50 μm. One of the fields (E_c) was delayed by a computer-controlled actuator. The other two fields (E_a and E_b) were overlapped in time and space and were kept unchanged during the experiments. Time zero for all transients is defined as the point at which all three fields are coincident in time. For negative delays, E_c arrives at the sample before the other two fields and for positive times E_c arrives after them. The signal beam was directed to a 0.27 m monochromator and detected with a photomultiplier tube. In all cases, data were collected at the central wavelength of the laser pulse, typically 622 nm. The signals were collected by a boxcar integrator and stored in a computer for analysis.

In order to optimize the initial alignment of the four-wave mixing setup, templates of the beam arrangement were made and used to ascertain that all beams were parallel before the focusing lens. A second harmonic crystal, KDP, of 0.1 mm thickness was placed at the focus to optimize the spatial and temporal overlap of the fixed beams. Once the third beam was overlapped in space, it was scanned in time until the FWM signal beam appeared. When all three incident pulses were overlapped in time and space, a matrix of equally spaced red and UV beams could be seen after the crystal. These were the result of all combinations of second-, third-, and higher-order wave mixing processes occurring at the crystal at their appropriate phase matching angles. After further optimization of spatial and temporal overlap for the FWM signal, the crystal was removed from the beam path.

All experiments were performed on 30–760 Torr of gases or neat vapors (when liquid samples were used) contained in a static quartz cells. Sweeping the time delay between the variable and the fixed fields yielded transients that reflect the temporal evolution of the dynamics. At each time

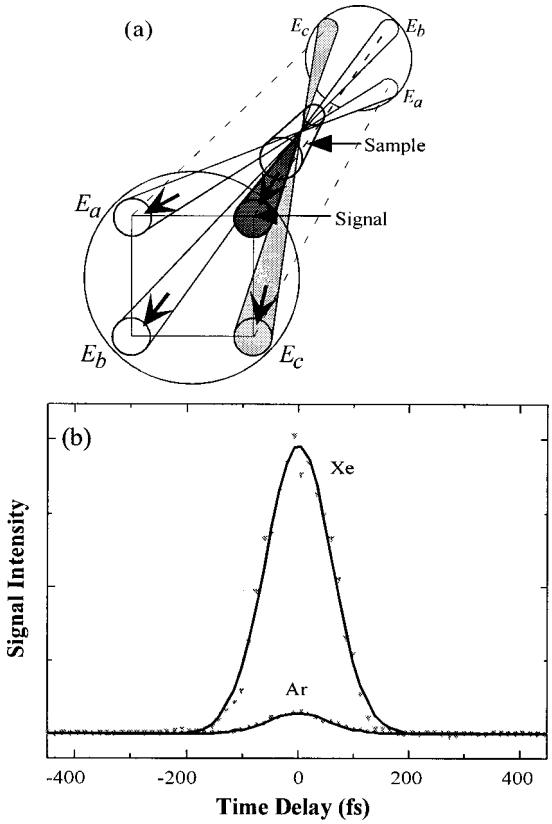

FIG. 3. (a) Beam arrangement in the forward box configuration (see Refs. 51 and 52). E_a and E_b are overlapped and fixed in time. For positive time delays, these fields set up a transient grating in the horizontal plane off which E_c Bragg scatters to give the FWM signal. The time delay between E_c and the two other fields is varied to obtain the time-dependent dynamics of the system. In our experiments, all beams were horizontally polarized. (b) FWM signal from xenon and argon samples at 1 atm pressure. The data are represented by triangles for Xe and by circles for Ar. The black lines show Gaussian fits to the data. FWM signal from Xe is 14 times greater than from Ar because of the increase in polarizability of Xe over Ar. The width of the Gaussian fit for Ar is 131 fs and 139 fs for Xe.

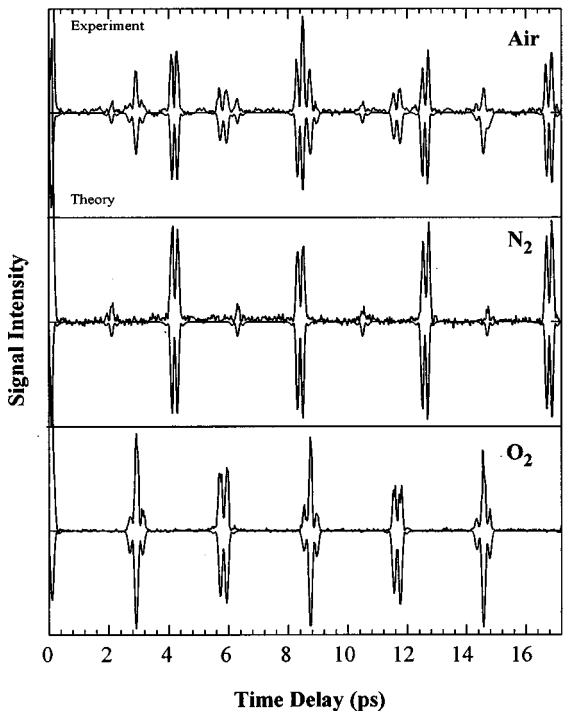

FIG. 4. Experimental and theoretical (shown as the negative mirror image of the experimental data) TG transients of air, nitrogen, and oxygen. Full rotational recurrences are observed at 4.15 ps for N_2 and at 5.77 ps for O_2. Half recurrences are also observed. The peaks in the air transient directly correspond to recurrences in the N_2 and O_2 scans. Simulated TG signals for these samples were calculated using Eq. (17). Note that in the simulations, the full and half recurrences are reproduced at the same recurrence times and with the same intensity and shape as in the experimental signal.

delay, the signal was collected for 10 laser shots; pulses with energy more than one standard deviation from the mean were discarded. Typical transients contain data from 150 different time delays and were averages of 10 scans. Care was exercised to minimize scattered light and to ensure that the collected signal was background free.

IV. RESULTS AND DISCUSSION

A. Atomic response

Transient grating data have been obtained for the atomic species argon and xenon at 1 atm pressure. The results are presented in Fig. 3(b). A single peak is observed in each scan which can be fit by a Gaussian function with the center at zero time delay and with a FWHM of 131 fs for Ar and 139 fs for Xe, corresponding to the third-order autocorrelation of our laser system. The FWM response of these samples is only present while the three laser pulses are temporally overlapped. At time zero, the intensity of the FWM signal from Xe is about 14 times stronger than that from Ar. The ratio between the linear polarizabilities of Xe and Ar is about 2.45.[93–95] This ratio appears to indicate a cubic dependence on the linear polarizability (α) for the time-zero signal. The signal observed at time zero results from a nonresonant instantaneous polarizability. The absence of the signal away from time zero is to be expected in spherically symmetric samples and in the absence of vibrations [see Eq. (17)].

B. Rotational contribution

The data in Fig. 4 (top) show the TG signal obtained for air. Even though these measurements are off-resonant, the nonlinear process responsible for the signal are similar to those illustrated in diagrams ab_g and ba_g in Fig. 2(a). The features in the air transient are interpreted as the rotational recurrences[96] of the constituent molecules of air.[97] TG transients for pure nitrogen and for pure oxygen, each at 1 atm pressure, were also taken. The results are also presented in Fig. 4 (middle and bottom) for comparison. Based on the rotational constants of nitrogen and oxygen (2.010 and 1.445 66 cm^{-1}, respectively) and the $\Delta J = \pm 2$ selection rule, full recurrences are expected and are observed at 4.15 and 5.77 ps intervals, respectively. Recurrences have a period of $(2\omega_J)^{-1}$; thus, half recurrences are expected at intervals $1/(8Bc)$ and full recurrences at $1/(4Bc)$. The alternation in heights between the half and full recurrences are caused by nuclear spin statistics. Whenever there is an interchange of equivalent nuclei in a rotation, the Pauli principle defines that only certain rotational states are populated. For molecules with a Σ_g^+ ground state, the ratio of the population of

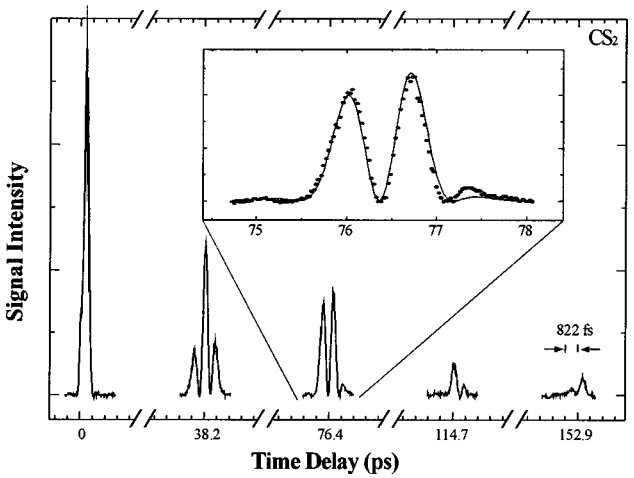

FIG. 5. TG transient of carbon disulfide. The half and full rotational recurrences are observed at 38.2 and 76.4 ps, respectively. The inset shows a magnification of the first full rotational recurrence (circles) with the simulation calculated using Eq. (17) (solid line). Notice that the *x*-axis is not continuous; there are 30 ps gaps between each recurrence and the tick size is 822 fs for each expanded region. The decrease in signal as a function of time delay gives the overall rotational dephasing due to inelastic collisions (see text).

odd J states to the population of even J states (nuclear statistics) is defined by $(I+1)/I$ for fermions and by $I/(I+1)$ for bosons where I is the nuclear spin.[82] Therefore, for N_2 with integral spin equal to one, even J states are populated twice as much as odd J states. The nuclear spin of O_2 is zero. However, because the ground state of O_2 is Σ_g^-, only odd J states are populated; whereas, for CS_2 with zero nuclear spin and ground state Σ_g^+, only even J states are populated.

All features in the transient in Fig. 4 can be identified and simulated using Eq. (17). In Fig. 4 the simulations appear as negative reflections of the experimental transients in the top, middle, and bottom sections. As can be seen in the figure, Eq. (17) predicts the rotational recurrences for N_2 and O_2 and the relative peak heights and shape in each half and full recurrence accurately. Because of the square in Eq. (17), TG transients look very different from LIF measurements.[19,67,68] By adding the simulated transients of N_2 and O_2, the experimental TG signal from air is reproduced.

Time-resolved TG experiments on carbon disulfide, CS_2 (300 Torr) yielded several transients showing multiple rotational recurrences, as depicted in Fig. 5. This molecule has been studied extensively using nonlinear techniques because of its high degree of nonlinear polarizability.[5,98–105] Its $\chi^{(3)}$ is 23×10^{-14} esu.[106] Heritage and co-workers observed short birefringence at 38 and 76 ps after excitation with a picosecond pulse and verified these positions for CS_2 theoretically.[5,107] The data in Fig. 5 allow accurate molecular constants to be extracted for this molecule. As can be seen, the half recurrence appears at 38.2 ps and the full recurrence occurs at 76.4 ps. For O_2, N_2, and CS_2, it is important to include centrifugal distortion in Eq. (17) to reproduce the TG signal well. In these cases, ω_J is replaced by $2\pi c[(4B-6D)(J+\frac{3}{2})-8D(J+\frac{3}{2})^3]$, where D is the centrifugal distortion constant. From the positions of the first two rotational recurrences, the rotational constant, $B=0.109\,12\pm0.000\,02\,\mathrm{cm}^{-1}$, and centrifugal distortion constant, $D=6.4\times10^{-9}\pm0.2\times10^{-9}\,\mathrm{cm}^{-1}$, are obtained for CS_2. The effective rotational constant, before the centrifugal distortion effect is incorporated, is $0.109\,07\pm0.000\,02\,\mathrm{cm}^{-1}$. From the literature, the rotational constant for CS_2 is $0.109\,10\ \mathrm{cm}^{-1}$ and the centrifugal distortion is $1.0\times10^{-8}\,\mathrm{cm}^{-1}$.[108]

The determination of highly accurate rotational constants for polyatomic species by time-resolved coherence techniques is by now a well-known method (see, for example, Refs. 96 and 20). Because these data were obtained over hundreds of picoseconds using a 0.25 m long translation stage with a resolution of 0.1 μm/step, the equivalent resolution in time delay can be estimated to be one part per million. In principle, this resolution translates into measurements of rotational constants with six significant digits. To experimentally achieve this accuracy, it is important to meticulously align and calibrate the translation stage, interferometrically or with a well-known standard, and to take into account the index of refraction of air at the wavelength of the laser fields.

The inset in Fig. 5 also shows a simulation of the first full recurrence calculated with Eq. (17) and the parameters obtained above. As can be seen in the figure, Eq. (17) reproduces the experimental signal well, missing only in the height of the last undulatory feature. The amplitude of the rotational recurrences in Fig. 5 was found to decrease exponentially. A fit to the average intensity of the rotational recurrences gives a single exponential decay corresponding to a dephasing time of 62 ± 5 ps. By comparison, using Raman-induced polarization spectroscopy (RIPS), Chen and coworkers obtained dephasing times of 175 ps and 154 ps for the smaller molecules O_2 and N_2, respectively.[97] The observed decay time for CS_2 implies a cross section for rotational dephasing of 4 nm^2 equivalent to a 11.3 Å diameter assuming hard sphere collisions.[97] This cross section appears to be very large and to depend on the rotational angular momentum, leading to the distortion of the rotational recurrences that is not accounted by the centrifugal term, especially those at later times in Fig. 5. This J dependent coherence relaxation is similar to the recent work on SF_6 published by Vasilenko *et al.*[109] A study of the inelastic collisions leading to the rotational coherence dephasing based on measurements at different pressures seems warranted.

C. Vibrational contribution

The TG transient obtained for mercuric iodide, HgI_2, heated to 280 °C (150 Torr), is presented in Fig. 6. Notice that the data contain a strong and broad feature near 500 fs with 211 fs oscillations. This feature is due to the rotational and vibrational coherence prepared in this large triatomic molecule. The Fourier transform of the experimental transient is shown as line (b) in the inset. The top Fourier transform (a) is obtained from the original experimental transient with the time-zero feature removed. As can be seen there are three major features in both transforms—one large peak at 19.7 ± 0.1 and a set of two peaks at 148.4 ± 0.2 and $167.9\pm0.2\,\mathrm{cm}^{-1}$. These peaks were fit with Gaussian functions to determine the center position and uncertainty. The sloping

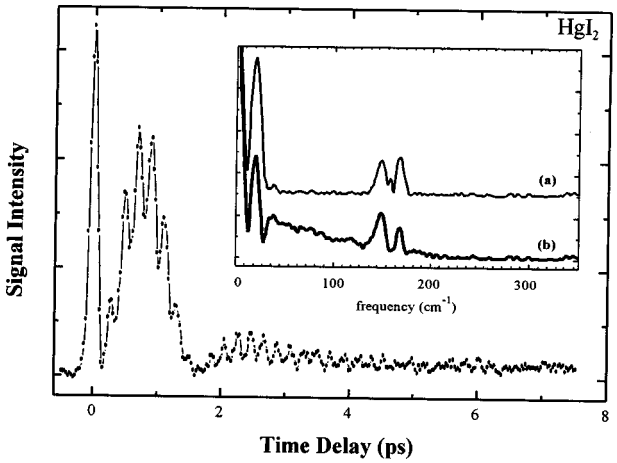

FIG. 6. (Bottom) TG transient of mercury (II) iodide. Ground state vibrations and rotations can clearly be seen in the transient. (Inset) The Fourier transform of the experimental transient is shown as line (b). The top Fourier transform (a) corresponds to the experimental transient with the coherence spike subtracted. The symmetric stretch of HgI_2 has a frequency of 158.2 cm^{-1}. The cross term resulting from Eqs. (13) and (16) causes the Fourier transform to have peaks corresponding to $2\omega_R$ ($19.7\pm0.1\,cm^{-1}$), $\omega_v-\omega_R$ ($148.4\pm0.2\,cm^{-1}$), and $\omega_v+\omega_R$, ($167.9\pm0.2\,cm^{-1}$) as seen. The $2\omega_v$ peak is probably masked by the high frequencies from the experimental noise and the relatively large point-to-point time steps.

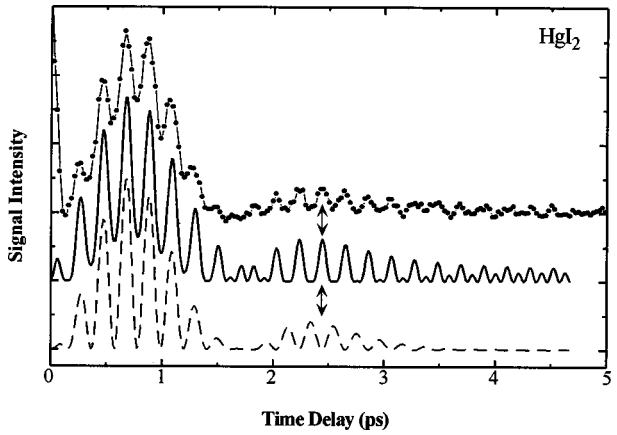

FIG. 7. (Top) Experimental TG transient of HgI_2. (Middle) Transient resulting from $\chi_{\alpha\alpha}(t)$ equal to the sum of $\chi^R(t)$ and $\chi^v(t)$. (Bottom) Transient resulting from $\chi_{\alpha\alpha}(t)$ equal to the product of $\chi^R(t)$ and $\chi^v(t)$. Notice that the product transient (bottom) is out-of-phase with the experimental data at 2.5 ps but the summation transient (middle) is in-phase with the experimental data for all times (see text).

feature at low frequencies in the raw Fourier transform (b) results from the time-zero coherence artifact; as can be seen in the upper Fourier transform, removing this time-zero spike by subtraction eliminates this sloping background and more clearly shows the three main features. A small peak (157.7 cm^{-1}) between the pair of peaks in (a) seems to appear as a result of removing the coherence artifact spike; this small peak is absent in the raw data Fourier transform. We checked the possibility that this small peak is due to a cross term between the first and second terms in Eq. (17). Our simulations did not support this argument probably because the equilibrium isotropic polarizability contributes only during the first 150 fs of the data. For experiments using nanosecond broad band lasers, this cross term becomes important.

The frequency exactly between the latter two peaks at $158.2\pm0.2\,cm^{-1}$ corresponds to the symmetric stretch, 158.4 cm^{-1} determined by gas-phase Raman spectroscopy.[110] Vibrational frequencies have also been obtained for gas-phase HgI_2 using electron diffraction yielding 156 cm^{-1} for the symmetric stretch, 235 cm^{-1} for the antisymmetric stretch, and 49 cm^{-1} for the bending mode.[111] As can be seen in Fig. 6, frequencies corresponding to the antisymmetric stretch and bending are not observed; these two modes are not Raman active in a linear triatomic molecule so bands for these normal modes should not be observed for HgI_2. The results from the Fourier transform will be discussed in more detail below.

As was shown above, Eq. (17) can been used to simulate the rotational dynamics for N_2, O_2, and CS_2. The HgI_2 data allow us to examine the separation of vibrational and rotational components in TG transients where the two are summed and to compare with the analysis of rotational anisotropy in pump–probe transients where the two are multiplied (see Sec. II C). Figure 7 shows the HgI_2 experimental data (top), a transient simulated by $\chi_{\alpha\alpha}(t)$ having a vibrational contribution of the formula given in Eq. (12) added to a rotational component according to Eq. (9), $\chi_{\alpha\alpha}(t)=\chi^v(t)+\chi^R(t)$ (middle), and a transient simulated by multiplying the vibrational and rotational components, $\chi_{\alpha\alpha}(t)=\chi^v(t)\chi^R(t)$ (bottom). As can be seen in the figure, the product of rotations and vibrations produces a series of oscillations that is out-of-phase with the experimental data between 1.7 and 4.5 ps. However, the sum of rotations and vibrations produces a series of oscillations that correspond in-phase to the vibrational oscillations of the data for all times.

The summation of the vibrational and rotational components of the polarizability provides the correct phase relationship in the data because of the cross term that is obtained from the square of the sum of sine functions. As is seen in the bottom simulation in Fig. 7, the effect of the cross term is to invert the phase of the vibrations near $\tau>1.7$ ps (see arrows at 2.5 ps) and to cause a doubling of the vibrational frequency for $\tau>3.5$ ps. The Fourier transform shown in Fig. 6 confirms the validity of this model. The Fourier transform should contain peaks corresponding to $2\omega_v$, $2\omega_R$, $\omega_v+\omega_R$, and $\omega_v-\omega_R$, where ω_R and ω_v are the average rotational and vibrational frequencies, respectively. Note that the square of the summation of sines also yields a constant term which causes a peak at zero frequency in the Fourier transform as seen in Fig. 6 for both transforms.

Looking at Fig. 6, a splitting around the symmetric stretching vibrational frequency ($\omega_v=158.2\,cm^{-1}$) is evident; thus $\omega_v-\omega_R$ (148.4 cm^{-1}) and $\omega_v+\omega_R$, (167.9 cm^{-1}) are obtained. In addition, there is a peak corresponding to $2\omega_R$ (19.7 cm^{-1}) reflecting the 1.7 ps modulation. This corresponds to twice the average rotational frequency that arises from the sum of all the rotational levels [third term in Eq. (17)]. The $2\omega_v$ peak, corresponding to periodic oscillations of 105.4 fs, is not observed. This is probably because of a lack of time resolution as determined by the FWHM of the coherent spike, 138 fs for this transient. It is also possible that χ^v is small compared to the other terms that enter Eq.

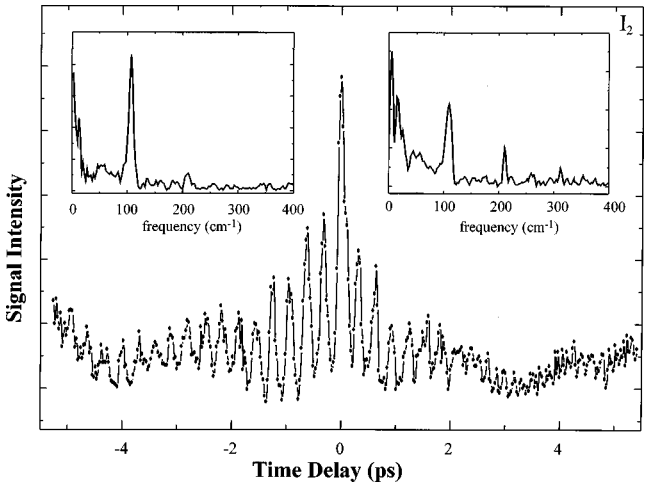

FIG. 8. (Bottom) TG and RTG transient of iodine. Vibrations can clearly be seen at both negative (left) and positive (right) time delays. Lasers with central wavelength of 622 nm are resonant with the $X \leftrightarrow B$ electronic transition. (Left inset) Fourier transform of the data at negative delay times. There is one main peak at $107.1 \pm 0.3\ \mathrm{cm}^{-1}$ and another smaller peak at $209.9 \pm 0.3\ \mathrm{cm}^{-1}$. (Right inset) Fourier transform of the data at positive delay times. The frequencies of the three main peaks are 107.8 ± 0.4, 210.8 ± 0.1, and $312.0 \pm 0.2\ \mathrm{cm}^{-1}$. Taking these values and accounting for the combination frequencies that should be observed in each Fourier transform because of the summation of cosines, values for the excited vibrational frequency ($105\ \mathrm{cm}^{-1}$), ground vibrational frequency ($208\ \mathrm{cm}^{-1}$), and average rotational frequency ($3\ \mathrm{cm}^{-1}$) can be obtained.

(17). The summation of the equilibrium anisotropic polarizability (responsible for rotational dynamics) and the derivative of the polarizability with respect to the vibrational coordinates is consistent with Raman scattering theory.[79,80] The HgI_2 experimental data confirms that the analysis of time-resolved molecular dynamics by TG requires a summation of rotational and vibrational components and this is in contrast to the analysis of time-resolved pump–probe transients.

Figure 8 presents TG (for positive time delay) and RTG (for negative time delay) data obtained from an iodine sample heated to 130 °C (160 Torr). Room temperature transients were also recorded but are not shown here. Unlike the previous experimental transients shown here, both excited and ground state dynamics of I_2 are observed. The difference stems from whether or not the TG interactions are resonant with the appropriate electronic transitions of the molecule in question. In this case, all three fields are resonant with transitions from the $X(^1\Sigma_g^+)$ and the $B(^3\Pi_{0^+u})$ states.[112–115] Transitions to other states with smaller transition probabilities at the wavelength of excitation, such as the A_{1u} state, are not observed because of the μ^8 dependence of the signal. All eight diagrams in Fig. 2 contribute to the observed signal. In Fig. 8, ground state and excited state dynamics are clearly obtained by TG with three 622 nm beams. Schmitt *et al.* have carried out CARS and DFWM measurements on this molecule showing both ground and excited state dynamics, evident in the Fourier transform of data from positive time delays.[10,12] Below we present the analyses of our iodine experimental data for positive and negative time delays separately.

For positive time delays (Fig. 8, right inset) the dynamics arise from wave packets formed in the ground state [diagrams ab_g and ba_g in Fig. 2(a)] and in the excited state [diagrams ab_e and ba_e in Fig. 2(b)]. It has been shown that vibrational levels $v' = 7-12$ form a coherent superposition in the B excited state following excitation with 620 nm pulses.[13,20,116,117] Each population in the ground and excited states contributes vibrational and rotational dynamics to the signal. To simulate the experimental data, it is best to explicitly include each frequency component in Eq. (17) (*vide infra*); however, for simplicity we can understand the data if we assume average frequencies for the excited and ground states. Thus we have two vibrational frequencies (ω_v'' and ω_v') and two rotational frequencies (ω_R'' and ω_R') which we know from the literature for the ground and excited states respectively.[112–115,118] When these four terms are introduced in Eq. (6), the squaring results in a total of 16 terms. The first four terms give dynamics proportional to $2\omega_R''$, $2\omega_R'$, $(\omega_R'' + \omega_R')$ and $|\omega_R'' - \omega_R'|$, all in the range of 0–50 cm^{-1}. The next four terms give frequencies proportional to $2\omega_v' \sim 220\ \mathrm{cm}^{-1}$, $2\omega_v'' \sim 420\ \mathrm{cm}^{-1}$ (not observed), $(\omega_v'' + \omega_v') \sim 310\ \mathrm{cm}^{-1}$ and $|\omega_v'' - \omega_v'| \sim 105\ \mathrm{cm}^{-1}$. The remaining eight terms correspond to the sums and differences arising from the four cross terms between vibrations and rotations. Because the rotational frequencies are very small compared to the vibrational frequencies only two peaks are expected, one at $\omega_v'' \sim 210\ \mathrm{cm}^{-1}$ and the other at $\omega_v' \sim 110\ \mathrm{cm}^{-1}$. The Fourier transform shows the low frequency rotational contributions and the three peaks at 107.8 ± 0.4, 210.8 ± 0.1, and $312.0 \pm 0.2\ \mathrm{cm}^{-1}$. Taking these values and accounting for the combination frequencies that should be observed in each Fourier transform because of the summation of cosines, values for the average excited vibrational frequency ($105\ \mathrm{cm}^{-1}$), average ground vibrational frequency ($208\ \mathrm{cm}^{-1}$), and average rotational frequency, $J_{\mathrm{ave}}B_{\mathrm{ave}}$ ($3\ \mathrm{cm}^{-1}$) can be obtained. Here B_{ave} is the average of the ground and excited rotational constants and J_{ave} is the average J level (≈ 100). These values agree well with the available spectroscopic data of I_2 for the ground and excited states.[112–115,118]

An accurate determination of the magnitude of each of the mentioned contributions is not possible with the available data. Typically the anisotropic equilibrium polarizability (leading to the observation of rotations) is larger than the derivative of the polarizability (vibrational dependence), therefore rotational-vibrational cross terms are expected to have a major contribution. Quantum calculations have also been performed in connection to the phase locked experiments by Scherer *et al.* on I_2, where the time dependence of the ground and excited state coherence was critical to their interpretation.[119] The ground state motion has been studied quantum-mechanically by Jonas *et al.*[120] and Smith *et al.*[121]

Based on the guidelines in Sec. II B, a semiempirical calculation [using Eq. (6)] can be performed that takes into account the rotational and vibrational contributions to the TG signal from ground and excited states as well as the coherent-coupling term, which contributes near time zero. In Fig. 9, we show the simulated transient and corresponding Fourier transforms. The calculated transient looks similar to the positive time experimental data. The Fourier transform shows peaks of similar position and shape to those obtained from the experimental data. The finite pulse duration in the experi-

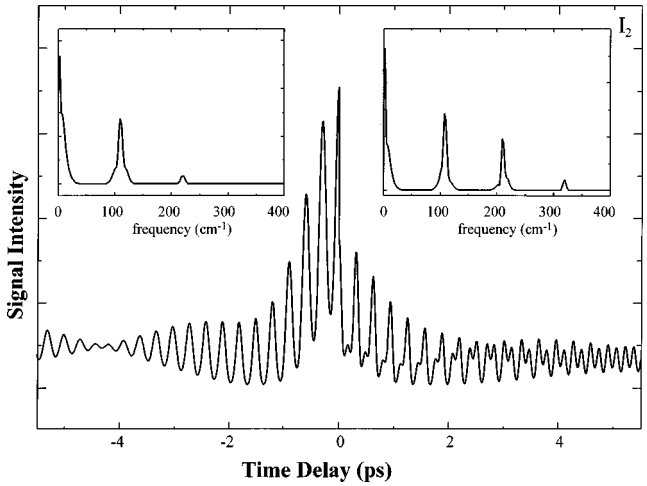

FIG. 9. Simulation of the iodine signal for positive and negative time delays (see text). The insets show the corresponding Fourier transforms. The simulations agree well with the experimental results presented in Fig. 8.

ments causes a loss of resolution for the high frequency components. We have not included convolution in the simulation; most likely this explains why the heights of the high frequency components are higher in the simulation Fourier transform than in the experimental one. If the parameters of the simulation, such as the magnitude and phase of each contribution ($v_B=7-12$ and $v_X=0-3$), were optimized by a fitting routine, an even better agreement could have been obtained.

The negative-time signal in Fig. 8 is observed when field E_c precedes fields E_a and E_b. Notice that the labels of the fields are arbitrary except for the fact that E_c is the only field that we delay or advance in time. The term ''negative time delay'' does not imply that E_c is scattered towards the detector before grating formation E_a and E_b has occurred. When E_c precedes the other two fields [see Fig. 1(e) corresponding to RTG and diagrams cb_g and cb_e in Fig. 2(d)], an electronic coherence between the ground and excited states is formed (see Sec. II). The time dependence of this electronic coherence created by E_c is probed by the formation of a transient grating by E_b and scattering of E_a from the grating into the direction of the signal detector. In the gas phase, the coherence persists for long times and yields coherence decay information. For I_2 at 130 °C we have measured $T_2=330$ ps. We have measured dephasing rates for TG and RTG setups as a function of temperature and density. This work will be published elsewhere.[39]

The Fourier transform of the negative time delay experimental transient shows frequencies in the 0–10 cm^{-1} range as well as a strong component at $107.1\pm0.3\,cm^{-1}$ and a weaker peak at $209.9\pm0.3\,cm^{-1}$ (Fig. 8, left inset). As indicated in Sec. II B, the coherence probed in the RTG measurement contains primarily a contribution from the excited state. This can be understood by considering the wave function launched by the first pulse as a coherent superposition of vibrational eigenfunctions from the ground and excited states. The signal is proportional to the overlap between the initial wave function $\Psi(t=0)$ and the wave function at later times $\Psi(t)$. For iodine the range of motion (center of mass) of the ground state components has been found to be 0.12 Å, while that of the B excited state is 0.6 Å and it is significantly displaced from the ground state equilibrium geometry.[116,120,121] Therefore, the signal observed is dominated by the dynamics on the excited state. This point was tested with a calculation of the overlap between two ground and excited state model oscillators and it is a manifestation of the Condon approximation.[37]

The rotational component of the signal depends on the rotational dynamics of the coherence. When the excited state vibrational dynamics, the time-zero component, and the rotational dephasing terms are introduced in Eq. (6), one obtains a transient that is very similar to the observed data. The simulated transient and its Fourier transform at negative time delays, shown in Fig. 9, are in good agreement with the experimental observations (Fig. 8). We will address different pulse sequences that lead to similar coherence dynamics and their more precise simulations in a future publication.[40]

Other sources for the negative time signal have been considered. Most importantly we can rule out the possibility of a two-photon resonant excitation by which other potential energy curves are probed. For gas-phase iodine the only two-photon allowed transition is to a repulsive state.[13,122] Repulsive states can only contribute to the observed signal within the first $\tau<100$ fs. In the liquid phase, the ion pair states of iodine are solvated and can be reached by two photons with wavelength in the visible. These states have been implicated in the studies from Fleming's group on phase locked dynamics of molecular iodine.[123] The contribution of ion pair states in the data presented here is ruled out because for gas-phase iodine three photons are required to reach them. Most importantly, the semiempirical calculations presented here, involving the B and X states closely reproduce the data and the corresponding Fourier transform. The observation of coherence dynamics for negative time delays in four-wave mixing has been discussed theoretically by Mukamel *et al.*[54,62,63] and has been observed in the gas phase by M. Schmitt *et al.* (for I_2) and by Motzkus *et al.* (for Na_2).[9,10]

D. Early time response and comparison to liquid data

The results presented in Fig. 10 compare the early time TG response for two gem-dihalomethane molecules, CH_2Cl_2 (340 Torr) and CH_2Br_2 (40 Torr). The two transients can be described by a time-zero coherence spike followed by a rotational coherence feature. As expected, based on the rotational moment of inertia, the dichloro compound has a faster rotational dephasing component. The dibromo compound is much slower. In both cases the rotational dephasing and time-zero coherence spike can be simulated using Eq. (17) and the rotational constants for these compounds are recuperated, 0.12 and 0.050 cm^{-1} for CH_2Cl_2 and CH_2Br_2, respectively. The rotational constants calculated from moments of inertia are 1.1, 0.106, and 1.10 cm^{-1} for CH_2Cl_2 and 0.88, 0.0412 and 0.041 cm^{-1} for CH_2Br_2.[124] The B rotational constants for each molecule are close to the values we found; however, because CH_2Cl_2 and CH_2Br_2 are not symmetric tops, the measured rotational constant is a combination of the three rotational constants. From these early time TG signals,

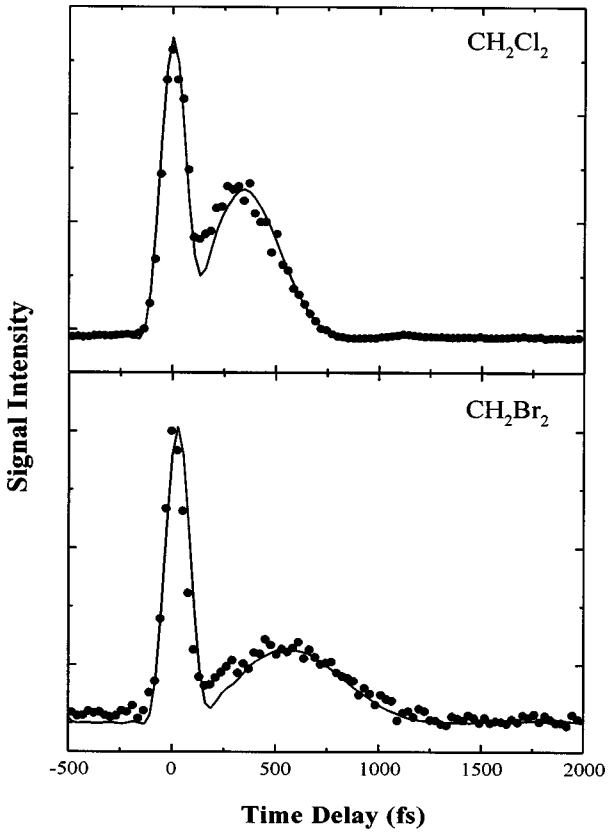

FIG. 10. TG transients of methylene chloride (upper) and methylene bromide (lower). The experimental data are shown as circles and the simulations calculated using Eq. (17) are shown by the solid line. In both scans, the time-zero coherence spike is observed and is more intense than the rotational dephasing. As expected, the rotational recurrence is faster in CH_2Cl_2 than in CH_2Br_2.

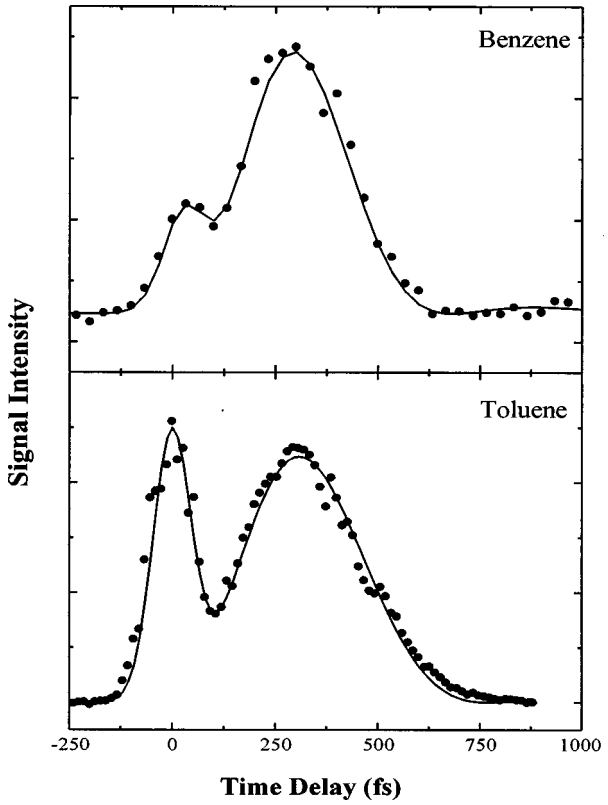

FIG. 11. TG transients of benzene (upper) and toluene (lower). The experimental data are shown as circles and the solid lines show the simulations from Eq. (17). The intensity of the rotational dephasing in benzene is stronger than the time-zero spike. However, in toluene the intensities of the rotational recurrence and the time-zero spike are about equal. The rotational recurrence time is similar for both compounds as expected from their rotational constants.

we observe that even in the absence of rotational recurrences, the initial dephasing is sufficient to determine the rotational constant of a molecule with two-digit accuracy or the rotational temperature of a known molecule or product of a reaction.

In addition to the rotational dephasing, the data on CH_2Br_2 contains a weak oscillatory modulation with a period of 190 fs. The frequency of this oscillation, confirmed by Fourier transformation of the data, corresponds to the Br–C–Br bending motion frequency around 173 cm^{-1}.[125] Impulsive stimulated Raman scattering measurements by Ruhman *et al.* on CH_2Br_2 have demonstrated the persistence of this bending motion for several picoseconds in the liquid phase.[126]

Figure 11 compares the early time TG response for larger polyatomic molecules, in this case benzene (90 Torr) and toluene (30 Torr). These molecules are highly polarizable with $\chi^{(3)}$ coefficients of 10.1 and 9.81×10^{-14} esu for benzene and toluene, respectively.[106] Simulations to the data using Eq. (17) yield rotational constants of 0.1896 for benzene and 0.146 cm^{-1} for toluene. In the literature, the three rotational constants for benzene are 0.189 60, 0.189 60, and 0.094 80 cm^{-1},[127] and for toluene are 0.191 06, 0.083 97, and 0.058 34 cm^{-1}.[128] Our rotational constant for benzene, an oblate symmetric top, is in excellent agreement with the literature value for *B*. Because toluene is not a symmetric top, the *B* value from the literature is not corresponding well with the value we determined. However, if the reduced moment of inertia is used to calculate the rotational constant for toluene,[124] the rotational constant becomes 0.146 cm^{-1} which does agree well with our value.

The femtosecond gas-phase CARS measurement by Hayden and Chandler on benzene gives the overall 12 ps rotational dephasing signal.[11] Our transient (in Fig. 11) gives the early (first 500 fs) dynamics where the initial rotational dephasing is observed; a subsequent oscillation of the rotational coherence has also been observed at 1.2 ps (not shown). The data of Hayden and Chandler show the 1.2 ps feature as well as one at 4 ps and one at 8 ps.[11]

In benzene, the rotational dephasing component of the signal is more intense than the coherent spike at time zero. A similar effect for the relative intensities of time zero and the rotational dephasing was also observed for CS_2 and is expected for molecules with large anisotropic polarizabilities. For toluene, the relative intensities of the coherent spike and the rotational dephasing are about equal. At time zero, the signal results from the coherence coupling artifact through the instantaneous polarizability of the equilibrium isotropic component as well as other combinations of interactions between the three electric fields as discussed in Sec. II; the anisotropic orientational dependence contribution $\chi^R(t)$ in Eq. (9) is zero at time zero. For positive times, only $\chi^R(t)$

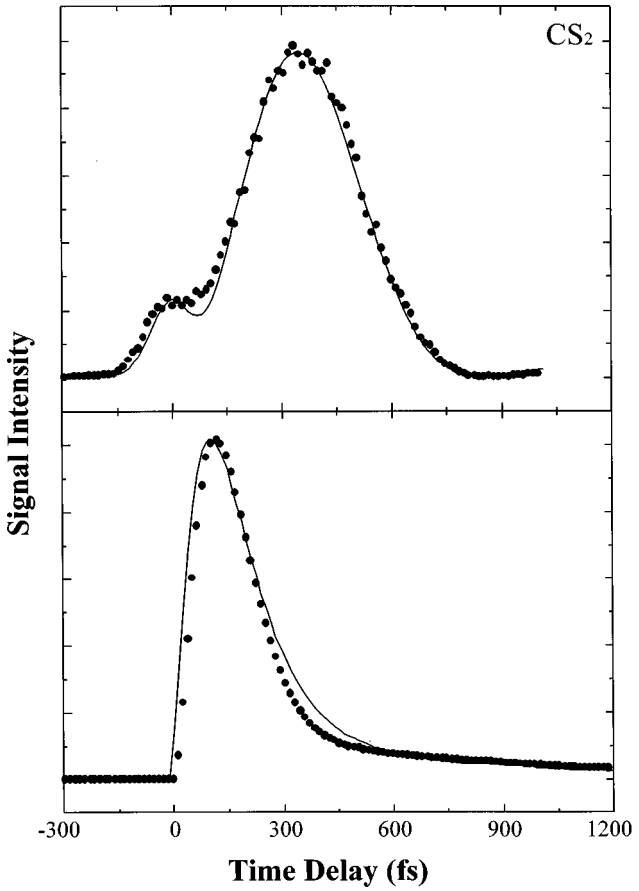

FIG. 12. (Top) TG transient obtained for CS_2 near time zero. The experimental data (circles) contain a very small coherence coupling artifact followed by a large rotational dephasing component. The data has been simulated using Eq. (17) as shown by the solid line. (Bottom) The curve with the circles corresponds to the simulation of our gas-phase TG signal for CS_2 multiplied by a fast decaying function which simulates inhomogeneous dephasing and by a slow decay function which simulates diffusional dephasing (see text). The smooth line corresponds to a simulation curve used by Nelson and co-workers to fit the liquid-phase experiments (see Refs. 27 and 129).

contributes to the TG signal observed for these off-resonant transients. Both normal mode dependent contributions, Eqs. (11a) and (11b), average to zero because of the very fast vibrational frequencies in comparison to the coherence length of our laser pulses. A further refinement of Eq. (17) that gives an explicit dependence for the intensity of the coherence coupling artifact amplitude, A, in terms of the various contributions may be the subject of a future publication.

The gas-phase measurements presented in this study provide the isolated molecular response of the material. When compared to condensed-phase measurements, one can immediately recognize the intermolecular influence on the polarizability of the system. In Fig. 12 (top) we present both the early time response of gas-phase CS_2 measured in our laboratory and the simulation from Eq. (17). In order to compare our data with liquid-phase measurements, we have simulated the data from Nelson's group on CS_2 obtained by impulsive stimulated Raman scattering using the same semiempirical formula used to simulate their data.[27,129] This simulation of the liquid data from Nelson's group is presented as the solid line in the bottom of Fig. 12. In their simulation three time scales were identified; (i) a fast component due to inhomogeneous dephasing, (ii) a fast emergence of an ensemble of aligned and coherently librating molecules, and (iii) a slow diffusional dephasing of the orientational anisotropy. The fast time constants in the simulation were given $1/e$ values of 114 and 102 fs, respectively, the slow diffusional dephasing was simulated by a time constant of 1.37 ps, and the coherence coupling artifact was ignored.[27,129] It is clear that the condensed-phase data has a fast initial dephasing rate followed by a much slower decaying component.

Based on the simulation of the gas-phase data, we have attempted to reconstruct the condensed-phase measurements. Our simulation is achieved by multiplying our gas-phase simulation for CS_2 [from Eq. (17)] with a function that includes both a fast decay time of 65 fs to simulate the inhomogeneous dephasing and a slow decaying component to incorporate the diffusive reorientational dephasing of 1.37 ps. The resulting curve, shown by the circles in the bottom of Fig. 12, is very similar to the one generated by Nelson and co-workers. The differences between the two curves are a slight delay in the peak of the transient and a dip at ~420 fs. These differences may provide a more accurate simulation to the data presented in their publication.[27,129] The position where the signal achieves its maximum value is very sensitive to the fast decay which simulates the inhomogeneous broadening. Liquid-phase measurements have found that upon dilution the inhomogeneous decay rate decreases because the CS_2–alkane interactions are weaker than those between CS_2 molecules.[103,130,131] These findings are consistent with a physical description in which a weakening of the intermolecular interactions leads to dynamics that more closely mimic a gas-phase environment. Based on our preliminary model, only the inhomogeneous dephasing rate would need to be modified to simulate such behavior. The preliminary analysis presented here indicates that gas-phase dynamics can be used to provide a starting point toward the simulation of liquid-phase dynamics, especially during the first picosecond before dephasing is complete.

V. CONCLUSIONS

In summary, we have presented several types of femtosecond dynamic responses from atomic, diatomic, and polyatomic gases. The nonlinear interactions between the laser fields and the sample have been sorted using double-sided Feynman diagrams. We have combined the quantum mechanical dependence of the molecular polarizability with the semiclassical expressions for the time-resolved rotational dynamics to arrive at a formula that describes the observed rotational dynamics in diatomic and polyatomic molecules as well as describing the vibrational dynamics. The experimental TG transients on atoms and molecules have been simulated using this formulation. The TG transient from air demonstrated the ability of Eq. (17) for simulating rotational recurrences. Furthermore, it also demonstrated the capabilities for using TG techniques in the analysis of multiple component mixtures such as N_2 and O_2. Using the CS_2 transient, we demonstrated the accuracy that this time-resolved technique can achieve in the measurement of rotational tempera-

ture, rotational constants, and centrifugal distortion directly from the time-dependent data without the need for Fourier transformation. For HgI_2, vibrational coherence from the symmetric stretch, which is the only Raman active mode, was observed. The cross terms arising from the sum of rotational and vibrational dependent terms on the molecular polarizability have been identified in the Fourier transform of the HgI_2 data. Vibrational and rotational dynamics from both the ground and *B* excited states of I_2 were obtained for positive time delays and are consistent with previous observations.[10,12] For negative time delays, corresponding to the RTG configuration, coherence dynamics for I_2 were observed and simulated. The early time responses of polyatomic molecules including benzene, toluene, and the dihalogenated methanes were investigated. The relative contribution from the anisotropic and isotropic components as defined by Eqs. (11a) and (11b) to each part of the FWM signal is still being examined in order to further refine Eq. (17) for different polarization arrangements. Finally, for molecules with large anisotropic polarizability, we showed that the rotational dephasing signal may be stronger than the time-zero coherence spike.

Note added in proof. We have obtained higher resolution data for I_2 which support our conclusions. We are also working on a full quantum simulation of these results. Results from these studies will be published elsewhere.[39–42]

ACKNOWLEDGMENTS

We thank Dr. Materny, Dr. Chandler, and Dr. Frey for early comments on their CARS and DFWM experiments. We are grateful that Professor S. Mukamel taught us the power of the double-sided Feynman diagrams, which are the key to understanding nonlinear optics. We appreciate scientific discussions with Misha Ivanov, Professors G. Blanchard, and N. F. Scherer, and helpful comments on the manuscript by J. A. Cina. We also want to thank the referee of this manuscript for insightful comments on the interpretation of these experiments. This work was partially funded by a Camille and Henry Dreyfus New Faculty Award. E.J.B. is supported by a National Science Foundation Graduate Fellowship. M.D. is a Packard Science and Engineering Fellow and a Beckman Young Investigator. Funding for this project comes from Grant No. CHE-9812584 of the National Science Foundation.

[1] *Femtochemistry*, edited by A. H. Zewail (World Scientific, Singapore, 1994), Vols. I and II.
[2] *Femtochemistry*, edited by J. Manz and L. Woste (VHS, Heidelberg, 1995), Vols. I and II.
[3] *Femtochemistry: Ultrafast Chemical and Physical Processes in Molecular Systems*, edited by M. Chergui (World Scientific, Singapore, 1996).
[4] J. Manz, in *Femtochemistry and Femtobiology*, edited by V. Sundstrom (World Scientific, Singapore, 1997).
[5] J. P. Heritage, T. K. Gustafson, and C. H. Lin, Phys. Rev. Lett. **34**, 1299 (1975).
[6] M. D. Fayer, Annu. Rev. Phys. Chem. **33**, 63 (1982).
[7] T. S. Rose and M. D. Fayer, Chem. Phys. Lett. **117**, 12 (1985).
[8] T. S. Rose, W. L. Wilson, G. Wackerle, and M. D. Fayer, J. Chem. Phys. **86**, 5370 (1987).
[9] M. Motzkus, S. Pedersen, and A. H. Zewail, J. Phys. Chem. **100**, 5620 (1996).
[10] M. Schmitt, G. Knopp, A. Materny, and W. Kiefer, Chem. Phys. Lett. **280**, 339 (1997).
[11] C. C. Hayden and D. W. Chandler, J. Chem. Phys. **103**, 10465 (1995).
[12] M. Schmitt, G. Knopp, A. Materny, and W. Kiefer, Chem. Phys. Lett. **270**, 9 (1997).
[13] R. M. Bowman, M. Dantus, and A. H. Zewail, Chem. Phys. Lett. **174**, 546 (1990).
[14] T. Baumert, V. Engel, C. Meier, and G. Gerber, Chem. Phys. Lett. **200**, 488 (1992).
[15] M. H. M. Jannsen, M. Dantus, H. Guo, and A. H. Zewail, Chem. Phys. Lett. **214**, 281 (1993).
[16] U. Marvet and M. Dantus, Chem. Phys. Lett. **256**, 57 (1996).
[17] Q. Zhang, U. Marvet, and M. Dantus, Faraday Discuss. **108**, 63 (1997).
[18] A. H. Zewail, in *Femtochemistry*, edited by J. Manz and L. Woste (VHS, Heidelberg, 1995), Vol. I.
[19] J. S. Baskin and A. H. Zewail, J. Phys. Chem. **98**, 3337 (1994).
[20] M. Gruebele and A. H. Zewail, J. Chem. Phys. **98**, 883 (1993).
[21] W. H. Hesselink and D. A. Wiersma, Phys. Rev. Lett. **43**, 1991 (1979).
[22] *Applications of Picosecond Spectroscopy to Chemistry*, edited by K. Eisenthal (Reidel, Dordrecht, 1984).
[23] G. R. Fleming, *Chemical Applications of Ultrafast Spectroscopy* (Oxford, New York, 1986).
[24] A. B. Myers and R. M. Hochstrasser, IEEE J. Quantum Electron. **QE-22**, 1482 (1986).
[25] K. Duppen and D. A. Wiersma, J. Opt. Soc. Am. B **3**, 614 (1986); D. A. Wiersma and K. Duppen, Science **237**, 1147 (1987).
[26] J. J. Kasinski, L. Gomez-Jahn, S. M. Gracewski, K. J. Faran, and R. J. D. Miller, J. Chem. Phys. **90**, 1253 (1989); L. Genberg, Q. Bao, S. Gracewski, and R. J. D. Miller, Chem. Phys. **131**, 81 (1989).
[27] Y.-X. Yan, L.-T. Cheng, and K. A. Nelson, in *Advances in Nonlinear Spectroscopy*, edited by R. J. H. Clark and R. E. Hester (Wiley, New York, 1987).
[28] J. Chesnoy and A. Mokhtari, Phys. Rev. A **38**, 3566 (1988).
[29] D. McMorrow, W. T. Lotshaw, and G. A. Kenney-Wallace, IEEE J. Quantum Electron. **QE-24**, 443 (1988).
[30] Nibbering, D. A. Wiersma, and K. Duppen, Phys. Rev. Lett. **66**, 2464 (1991).
[31] U. Banin, A. Waldman, and S. Ruhman, J. Chem. Phys. **96**, 2416 (1992).
[32] N. F. Scherer, L. D. Ziegler, and G. R. Fleming, J. Chem. Phys. **96**, 5544 (1992).
[33] M. Cho, S. J. Rosenthal, N. F. Scherer, L. D. Ziegler, and G. R. Fleming, J. Chem. Phys. **96**, 5033 (1992).
[34] L. Dhar, J. A. Rogers, and K. A. Nelson, Chem. Rev. **94**, 157 (1994).
[35] S. Meyer, M. Schmitt, A. Materny, W. Kiefer, and V. Engel, Chem. Phys. Lett. **281**, 332 (1997).
[36] S. Meyer, M. Schmitt, A. Materny, W. Kiefer, and V. Engel, Chem. Phys. Lett. **287**, 753 (1998).
[37] S. Mukamel, *Principles of Nonlinear Optical Spectroscopy* (Oxford, New York, 1995).
[38] T.-S. Yang, R. Zhang, and A. Myers, J. Chem. Phys. **100**, 8573 (1994).
[39] V. Lozovoy, I. Pastirk, and M. Dantus (to be submitted).
[40] E. J. Brown, I. Pastirk, I. Grimberg, V. Lozovoy, and M. Dantus (to be submitted).
[41] I. Pastirk, V. Lozovoy, E. J. Brown, I. Grimberg, and M. Dantus (to be submitted).
[42] I. Pastirk, V. Lozovoy, I. Grimberg, E. J. Brown, and M. Dantus (to be submitted).
[43] Y. R. Shen, *The Principle of Nonlinear Optics* (Wiley, New York, 1984).
[44] R. L. Abrams, J. F. Lam, R. C. Lind, D. G. Steel, and P. F. Liao, in *Optical Phase Conjugation*, edited by R. A. Fisher (Academic, New York, 1983).
[45] H. J. Eichler, P. Gunter, and D. W. Pohl, *Laser-Induced Dynamic Gratings* (Springer, Berlin, 1986).
[46] A. M. Weiner, S. D. Silvestri, and E. P. Ippen, J. Opt. Soc. Am. B **2**, 654 (1985).
[47] C. J. Bardeen and C. V. Shank, Chem. Phys. Lett. **203**, 535 (1993).
[48] D. T. Leeson, O. Berg, and D. A. Wiersma, J. Phys. Chem. **98**, 3913 (1994).
[49] T. Joo, Y. W. Jia, and G. R. Fleming, J. Chem. Phys. **102**, 4063 (1995).
[50] P. Vohringer, D. C. Arnett, T. S. Yang, and N. F. Scherer, Chem. Phys. Lett. **237**, 387 (1995).
[51] Y. Prior, Appl. Opt. **19**, 1741 (1980).
[52] J. A. Shirley, R. J. Hall, and A. C. Eckbreth, Opt. Lett. **5**, 380 (1980).
[53] S. Williams, R. N. Zare, and L. A. Rahn, J. Chem. Phys. **101**, 1072 (1994).

[54] W. M. Zhang, V. Chernyak, and S. Mukamel, J. Chem. Phys. (submitted).
[55] S. Mukamel, M. Cho, and G. R. Fleming, J. Chem. Phys. **98**, 5314 (1993).
[56] P. H. Vaccaro, in *Nonlinear Spectroscopy for Molecular Structure Determination*, edited by E. Hirota, R. W. Field, J. P. Maier, and S. Tsuchiya (Blackwell Scientific, London, 1997).
[57] J. J. Sakurai, *Modern Quantum Mechanics*, revised ed. (Addison–Wesley, Reading, 1994).
[58] G. C. Schatz and M. A. Ratner, *Quantum Mechanics in Chemistry* (Prentice–Hall, Englewood Cliffs, 1993).
[59] T. Joo, Y. Jia, J.-Y. Yu, M. J. Lang, and G. R. Fleming, J. Chem. Phys. **104**, 6089 (1996).
[60] P. H. Vaccaro, in *Molecular Dynamics and Spectroscopy by Stimulated Emission Pumping*, edited by H.-L. Dai and R. W. Field (World Scientific, Singapore, 1995).
[61] Except for the phase-conjugate arrangement which is similar to a backward box configuration that has been limited to one plane. See Ref. 44 also.
[62] J. A. Leegwater and S. Mukamel, J. Chem. Phys. **101**, 7388 (1994).
[63] T. Meier, V. Chernyak, and S. Mukamel, J. Chem. Phys. **107**, 8759 (1997).
[64] G. R. Fleming and M. H. Cho, Annu. Rev. Phys. Chem. **47**, 109 (1996).
[65] Y. J. Yan and S. Mukamel, J. Chem. Phys. **94**, 179 (1991).
[66] R. N. Zare, *Angular Momentum. Understanding Spatial Aspects in Chemistry and Physics* (Wiley, New York, 1988).
[67] A. H. Zewail, J. Chem. Soc., Faraday Trans. 2 **85**, 1221 (1989).
[68] M. Dantus, R. M. Bowman, J. S. Baskin, and A. H. Zewail, Chem. Phys. Lett. **159**, 406 (1989).
[69] M. Cho, M. Du, N. F. Scherer, G. R. Fleming, and S. Mukamel, J. Chem. Phys. **99**, 2410 (1993).
[70] M. Cho, G. R. Fleming, and S. Mukamel, J. Chem. Phys. **98**, 5314 (1993).
[71] M. Morgen, W. Price, P. Ludowise, and Y. Chen, J. Chem. Phys. **102**, 8780 (1995).
[72] A. B. Myers and R. M. Hochstrasser, J. Chem. Phys. **85**, 6301 (1986).
[73] T. Joo and A. C. Albrecht, Chem. Phys. **173**, 17 (1993).
[74] S. A. Schaertel, D. Lee, and A. C. Albrecht, J. Raman Spectrosc. **26**, 889 (1995).
[75] H. Li and W. Kong, J. Chem. Phys. **107**, 3774 (1997).
[76] T. A. W. Wasserman, P. H. Vaccaro, and B. R. Johnson, J. Chem. Phys. **106**, 6314 (1997).
[77] T. Muller, T. A. W. Wasserman, P. H. Vaccaro, and B. R. Johnson, J. Chem. Phys. **108**, 4 (1998).
[78] T. A. Wasserman, P. H. Vaccaro, and B. R. Johnson, J. Chem. Phys. **108**, 7713 (1998).
[79] D. A. Long, *Raman Spectroscopy* (McGraw–Hill, New York, 1977).
[80] D. A. Long, in *Nonlinear Raman Spectroscopy and Its Chemical Applications*, edited by W. Kiefer and D. A. Long (Reidel, Dordrecht, 1982).
[81] R. G. Gordon, J. Chem. Phys. **45**, 1643 (1966).
[82] G. Herzberg, *Molecular Spectra and Molecular Structure. II. Infrared and Raman Spectra of Polyatomic Molecules*, 11th ed. (Van Nostrand, New York, 1945).
[83] E. B. Wilson, J. C. Decius, and P. C. Cross, *Molecular Vibrations* (Dover, New York, 1955).
[84] F. A. Cotton, *Chemical Applications of Group Theory*, 2nd ed. (Wiley, New York, 1963).
[85] A. Baltuska, Z. Y. Wei, M. S. Pshenichnikov, and D. A. Wiersma, Opt. Lett. **22**, 102 (1997).
[86] M. Nisoli, S. DeSilvestri, O. Svelto, R. Szipocs, K. Ferencz, C. Spielmann, S. Sartania, and F. Krausz, Opt. Lett. **22**, 522 (1997).
[87] H. E. Lessing and A. von Jena, in *Laser Handbook*, edited by M. L. Stich (North–Holland, Amsterdam, 1979), Vol. 3.
[88] B. S. Wherrett, A. L. Smirl, and T. F. Boggess, IEEE J. Quantum Electron. **QE-19**, 680 (1983).
[89] T. F. Heinz, S. L. Palfrey, and K. B. Eisenthal, Opt. Lett. **9**, 359 (1984).
[90] R. A. Engh, J. W. Petrich, and G. R. Fleming, J. Phys. Chem. **89**, 618 (1985).
[91] P. M. Felker, J. S. Baskin, and A. H. Zewail, J. Phys. Chem. **90**, 724 (1986).
[92] J. S. Baskin, P. M. Felker, and A. H. Zewail, J. Chem. Phys. **84**, 4708 (1986).
[93] Y. Liang, S. Augst, S. L. Chin, Y. Beaudoin, and M. Chaker, J. Phys. B **27**, 5119 (1994).
[94] F. London, Trans. Faraday Soc. **33**, 8 (1937).
[95] C. Hattig and B. A. Hess, J. Phys. Chem. **100**, 6243 (1996).
[96] P. M. Felker and A. H. Zewail, in *Femtosecond Chemistry*, edited by J. Manz and L. Woste (Verlag Chemie GmbH, Weinheim, 1995).
[97] M. Morgen, W. Price, L. Hunziker, P. Ludowise, M. Blackwell, and Y. Chen, Chem. Phys. Lett. **209**, 1 (1993).
[98] E. P. Ippen and C. V. Shank, Appl. Phys. Lett. **26**, 92 (1975).
[99] B. I. Greene and R. C. Farrow, J. Chem. Phys. **77**, 4779 (1982).
[100] B. I. Greene and R. C. Farrow, Chem. Phys. Lett. **98**, 273 (1983).
[101] M. Golombok, Kenney-Wallace, and S. C. Wallace, J. Phys. Chem. **89**, 5160 (1985).
[102] C. Kalpouzos, W. T. Lotshaw, D. McMorrow, and G. A. Kenney-Wallace, J. Phys. Chem. **91**, 2028 (1987).
[103] C. Kalpouzos, D. McMorrow, W. T. Lotshaw, and G. A. Kenney-Wallace, Chem. Phys. Lett. **150**, 138 (1988).
[104] Y. J. Chang, P. Cong, and J. D. Simon, J. Phys. Chem. **99**, 7857 (1995).
[105] T. Lian, Y. Kholodenko, B. Locke, and R. M. Hochstrasser, J. Phys. Chem. **99**, 7272 (1995).
[106] G. R. Meredith, B. Buchalter, and C. Hanzlik, J. Chem. Phys. **78**, 1533 (1983).
[107] C. H. Lin, J. P. Heritage, T. K. Gustafson, R. Y. Chiao, and J. P. McTague, Phys. Rev. A **13**, 813 (1976).
[108] G. Herzberg, *Molecular Spectra and Molecular Structure. III. Electronic Spectra and Electronic Structure of Polyatomic Molecules* (Van Nostrand Company, New York, 1966).
[109] L. S. Vasilenko, N. N. Rubtsova, and E. B. Khvorostov, Zh. Eksp. Teor. Fiz. **113**, 826 (1998) [JETP **86**, 450 (1998)].
[110] R. J. H. Clark and D. M. Rippon, J. Chem. Soc., Faraday Trans. 2 **69**, 1496 (1973).
[111] V. P. Spiridonov, A. G. Gershikov, and B. S. Butayev, J. Mol. Struct. **52**, 53 (1979).
[112] R. N. Zare, J. Chem. Phys. **40**, 1934 (1964).
[113] J. I. Steinfeld, R. N. Zare, L. Jones, M. Lesk, and W. Klemperer, J. Chem. Phys. **42**, 25 (1965).
[114] R. J. LeRoy, J. Chem. Phys. **52**, 2683 (1970).
[115] J. Tellinghuisen, J. Quant. Spectrosc. Radiat. Transf. **19**, 149 (1978).
[116] M. Gruebele, G. Roberts, M. Dantus, R. M. Bowman, and A. H. Zewail, Chem. Phys. Lett. **166**, 459 (1990).
[117] M. Dantus, R. M. Bowman, and A. H. Zewail, Nature (London) **343**, 737 (1990).
[118] G. Herzberg, *Molecular Spectra and Molecular Structure. I. Spectra of Diatomic Molecules* (Van Nostrand Company, New York, 1950).
[119] N. F. Scherer, R. J. Carlson, A. Matro, M. Du, A. J. Ruggiero, V. Romero-Rochin, J. A. Cina, G. R. Fleming, and S. A. Rice, J. Chem. Phys. **95**, 1487 (1991).
[120] D. M. Jonas, S. E. Bradforth, S. A. Passino, and G. R. Fleming, J. Phys. Chem. **99**, 2594 (1995).
[121] T. Smith, L. W. Ungar, and J. A. Cina, J. Lumin. **58**, 66 (1994).
[122] R. K. Sander and K. R. Wilson, J. Chem. Phys. **63**, 4242 (1975).
[123] N. F. Scherer, D. M. Jonas, and G. R. Fleming, J. Chem. Phys. **99**, 153 (1993).
[124] C. J. Reid and M. W. Evans, J. Chem. Soc., Faraday Trans. 2 **75**, 1218 (1979).
[125] *DMS Raman/IR Atlas*, edited by B. Schrader and W. Meier (Verlag Chemie GmbH, Wienheim, 1974).
[126] S. Ruhman, A. G. Joly, and K. A. Nelson, J. Chem. Phys. **86**, 6563 (1987).
[127] S. N. Thakur and L. Goodman, J. Chem. Phys. **78**, 4356 (1983).
[128] R. Vasudev and J. C. D. Brand, Chem. Phys. **37**, 211 (1979).
[129] S. Ruhman, L. R. Williams, A. G. Joly, B. Kohler, and K. A. Nelson, J. Phys. Chem. **91**, 2237 (1987).
[130] W. T. Lotshaw, D. McMorrow, N. Thantu, J. S. Melinger, and R. Kitchenham, J. Raman Spectrosc. **26**, 571 (1995).
[131] D. McMorrow, N. Thantu, J. S. Melinger, S. K. Kim, and W. T. Lotshaw, J. Phys. Chem. **100**, 10389 (1996).